Research Square

Preprints are preliminary reports that have not undergone peer review.
They should not be considered conclusive, used to inform clinical practice,
or referenced by the media as validated information.

A CPP-Functionalized LNP Platform for Oral Baculovirus DNA Delivery Enables Precision Control of Invasive Pests

Wen Zhao
Guangdong Academy of Sciences
Wen-Hao Hu
Guangdong Academy of Sciences
Tao Lin
Guangdong Academy of Sciences
Zi-Shang Li
Guangdong Academy of Sciences
Hui-Lan Mo
Guangdong Academy of Sciences
Ye-Pin Yu
Guangdong Academy of Sciences
Ping Hu
Guangxi Colleges and Universities Key Laboratory for Cultivation and Utilization of Subtropical Forest Plantation, Guangxi University
Ben-Shui Shu
Zhongkai University of Agriculture and Engineering
Jian-Ting Fan
National Joint Local Engineering Laboratory for High- Efficient Preparation of Biopesticide, Zhejiang A&F University
Ding-Ze Mang
Hebei University
Chang-You Li
Qingdao Agricultural University
Hong-Liang Yao
Guangdong Academy of Sciences
Rui Tang
tangr@giz.gd.cn

Guangdong Academy of Sciences

Research Article

Keywords: Lipid nanoparticles (LNPs), Cell-penetrating peptide (CPP), Selective organ targeting (SORT), Nucleopolyhedrovirus DNA, Precision pest management

Posted Date: September 1st, 2026

DOI: https://doi.org/10.21203/rs.3.rs-10655410/v1

License: This work is licensed under a Creative Commons Attribution 4.0 International License. Read Full License

Additional Declarations: No competing interests reported.

Abstract

Lipid nanoparticles (LNPs) have revolutionized nucleic acid delivery in human medicine, yet their potential in agricultural pest control remains largely unexplored. Here, we repurpose a clinical-stage selective organ targeting (SORT) LNP platform for the oral delivery of baculovirus DNA. By integrating a cell-penetrating peptide (CPP) and a SORT molecule into a single nanocarrier, we establish a versatile platform for precision invasive pest management. The SORT-CPP synergy was engineered to overcome the dual barriers of the insect gut: CPP enables active translocation across the peritrophic matrix, while the SORT molecule dictates endosomal escape in the alkaline midgut environment. Using the fall webworm (Hyphantria cunea) and its baculovirus (HcNPV) as a stringent model, we show that this DNAHcNPV@LNP-CPP-SORT platform achieves robust intracellular delivery. In Sf9 and S2 cells, the formulation overrode cellular barriers even in non-host contexts, confirming its capacity to bypass host restriction barriers. In vivo, viral gene expression was upregulated up to 20-fold within 24 h of oral inoculation, with histopathology revealing accelerated disruption of the peritrophic matrix. In parallel with this rapid viral accumulation, indoor bioassays demonstrated markedly expedited larval mortality. Field trials achieved larval population reductions of up to 77.9%, representing approximately 50% higher control efficiency compared to native HcNPV. Crucially, the platform exhibited species-selective enhancement, potentiating virulence against H. cunea without affecting non-target arthropods, and maintained excellent vertebrate biosafety. This work represents the first translation of clinical SORT-LNP technology into a field-ready biocontrol platform, expanding the operational paradigm of LNP technology beyond mammalian systems.

1 Introduction

Baculoviruses occupy a unique niche in pest management: they are exquisitely host-specific, environmentally benign, and leave no toxic chemical residues [1, 2]. Yet despite these virtues, their field performance remains constrained by two persistent bottlenecks: a slow speed of kill and an inherently narrow host range [3]. Wild-type nucleopolyhedroviruses (NPVs) partially mitigate environmental degradation through their occlusion bodies, which are crystalline protein matrices that shield virions from UV inactivation [4, 5]. Yet foliar-applied NPVs still exhibit a half-life of merely 20 to 25 hours on sun-exposed crop leaves [6]. Moreover, this natural protection is entirely lost once the viral genome is extracted for nanocarrier encapsulation: naked viral DNA is acutely vulnerable to nucleolytic degradation in the insect gut, a challenge well documented for orally delivered nucleic acids [7]. This paradox arises from the fact that the unmatched target specificity of baculoviruses is accompanied by practical limitations in both the intact virus and the isolated DNA forms. The root cause is a single fundamental bottleneck: inefficient delivery of viral genetic material across the formidable barriers of the insect midgut.

To initiate systemic infection, baculovirus occlusion-derived virions must sequentially traverse the peritrophic matrix, a chitinous mesh that filters macromolecules from the gut lumen, and the apical membrane of midgut epithelial cells [1, 4]. While wild-type viruses rely on a conserved set of per os

infectivity factors (PIFs) and associated envelope proteins to mediate these sequential entry events, the efficiency of primary oral infection remains intrinsically limited, restricting infectivity and contributing to delayed mortality and a narrow host range [8]. Efforts to enhance baculovirus performance through formulation additives or genetic modification have improved efficacy in specific settings but have not fundamentally overcome the intrinsic barriers to oral infection. The fundamental problem has remained unchanged: the virion must navigate both obstacles with only its native envelope proteins as guides. What is needed is not a better virus, but a fundamentally different strategy to breach the gut barrier.

The application of nanotechnology to agricultural pest management has advanced considerably in recent years, driven in large part by efforts to enable RNA interference (RNAi)-based crop protection [9-11]. Engineered nanocarriers have proven capable of delivering double-stranded RNA to silence essential genes in target insects [12], and mesoporous silica-based systems have improved the foliar persistence and controlled release of conventional chemical insecticides [7, 13]. These advances, however, have been confined predominantly to two cargo classes: small RNA molecules and small-molecule chemical actives [14, 15]. The delivery of large, functional DNA molecules, particularly complete viral genomes exceeding 100 kilobases, remains fundamentally uncharted territory in agriculture. The concept of using synthetic nanocarriers to deliver baculovirus DNA has been explored in a single precedent [16], which established that bypassing viral receptor dependency is feasible in principle. That study, however, employed non-degradable synthetic polymers without a clear translational pathway, leaving open the question of whether a clinically validated, biodegradable delivery platform could achieve the same effect with greater precision and safety. The vast potential of clinically validated LNP systems, which have transformed nucleic acid delivery in human medicine, therefore remains untapped for agricultural DNA delivery.

The modular design of lipid nanoparticles has quietly reshaped the landscape of nanomedicine over the past decade [17, 18]. Selective organ targeting (SORT) technology exemplifies this evolution: by simply tuning the chemistry and amount of a charged SORT molecule incorporated into the LNP formulation [19], the same core platform can be programmed for tissue-specific mRNA delivery or for enhanced intracellular functions such as endosomal escape [20]. This inherent versatility, validated across diverse ionizable lipids and nucleic acid cargoes, has established SORT-LNPs as one of the most clinically mature and adaptable delivery systems available [21]. In a parallel yet largely disconnected trajectory, cell-penetrating peptides (CPPs) have been extensively developed as molecular ligands capable of facilitating active translocation across biological barriers [22]. Recent authoritative perspectives have identified peptide–lipid hybrid platforms as a key frontier for next-generation nucleic acid delivery, underscoring the timeliness and potential of such functional integration [23]. Despite decades of research on each modality, the deliberate fusion of CPP and SORT functionalities into a single, integrated nanoparticle platform has remained unexplored—and their collective potential beyond mammalian systems, particularly for agricultural applications, has never been tested.

Unlike conventional formulations, LNPs are not fixed materials but modular delivery platforms whose biological behavior can be predictably reprogrammed by altering individual functional components. We

therefore reasoned that a clinical-stage SORT-LNP platform, originally engineered for programmable nucleic acid delivery in mammals, could be repurposed to address the oral delivery bottleneck that has long constrained baculovirus biopesticides. To test this hypothesis, we selected the fall webworm (*Hyphantria cunea*) and its cognate nucleopolyhedrovirus (HcNPV) as a stringent model: native infection, although ultimately lethal, is hampered by exactly the slow onset and inefficient DNA bioavailability that our nanocarrier is designed to overcome. By equipping a single LNP with both a cell-penetrating peptide (CPP) to breach the peritrophic matrix and midgut epithelium, and a SORT molecule to promote endosomal escape within the alkaline gut environment, we show that this dual-functional platform converts an otherwise inefficient oral DNA delivery process into one that is robust and biologically productive. The resulting gains in the speed of viral gene expression and the onset of larval mortality translate into meaningful improvements in field-level pest suppression, while the platform retains strong selectivity for the target pest and excellent biosafety in non-target organisms. This work demonstrates that clinical LNP technologies, when appropriately re-engineered for agricultural targets, can move beyond their original medical scope to enable a new class of precision nucleic acid pesticides.

2 Results and Discussion

2.1 Materials design, synthesis, and characterization

The DNA^{HcNPV}@LNP-CPP-SORT platform is constructed via self-assembly of three functional modules: a lipid-based skeletal matrix that provides structural integrity, a dual-ligand surface layer comprising CPP and the SORT molecule DOTAP that collectively enables gut barrier penetration and endosomal escape, and the encapsulated HcNPV genomic DNA payload (Figure 1A). The system is built upon the clinically validated ionizable lipid DLin-MC3-DMA [24], co-formulated with DSPC and cholesterol to form the lipid skeleton [25]. A DSPE-PEG$_{2000}$-maleimide (Mal) anchor is incorporated to enable covalent conjugation of the cell-penetrating peptide C105Y (sequence: CSIPPEVKFNKPFVYLI) via thioether linkage [26], while the permanently cationic lipid DOTAP is embedded within the lipid bilayer as the SORT molecule [19]. This dual-functional design is engineered to address two sequential barriers to oral baculovirus delivery: the CPP moiety facilitates active translocation across the peritrophic matrix and midgut epithelium, whereas the SORT molecule DOTAP promotes endosomal escape within the alkaline environment of the insect midgut.

Conjugation of C105Y to DSPE-PEG$_{2000}$-Mal was achieved through a Michael addition reaction, catalyzed by DIEA in DMF under nitrogen for 2 h, followed by dialysis (Figure 1B). Successful coupling was confirmed by ^{1}H NMR spectroscopy: the disappearance of characteristic H-a of C105Y (δ 2.5 ppm) and the concomitant disappearance of the maleimide proton signal H-1 (δ 6.88 ppm) collectively indicate quantitative thioether bond formation (Figure 1C–E). Fourier-transform infrared (FTIR) spectroscopy provided further structural validation—the DSPE-PEG$_{2000}$-C105Y conjugate retains both the C–O–C stretching vibration of the PEG backbone (~1100 cm^{-1}) and the amide I band of the peptide backbone (~1650 cm^{-1}), confirming the integrity of both components (Figure 1F).

The identity of the HcNPV stock was verified by PCR amplification of two genomic marker genes, *polyhedron* and *pe38*. Agarose gel electrophoresis revealed amplification products migrating at 281 bp and 994 bp, respectively, in exact agreement with predicted product sizes according to primer design (Figure 1G, Table S1). This result confirms the presence of intact HcNPV genomic DNA in the viral stock, thereby ensuring a reliable source material for subsequent extraction and encapsulation.

Both blank LNP-C105Y and DNA^{HcNPV}@LNP-C105Y-SORT displayed a pronounced Tyndall effect (Figure 1H) and exhibited uniform spherical morphology under transmission electron microscopy (TEM, Figure 1I–J), indicative of stable colloidal dispersion at the nanoscale [27]. Quantitative dynamic light scattering (DLS) analysis revealed that blank LNP-C105Y possess an average hydrodynamic diameter of 97.74 ± 1.11 nm, which increases significantly to 155.03 ± 3.88 nm upon encapsulation of the HcNPV genomic DNA (Figure 1I–K). The resulting diameter of 155.03 nm—substantially smaller than that of free baculovirus DNA—indicates effective compaction and internal encapsulation of the nucleic acid payload, consistent with the known capacity of ionizable lipid matrices to condense large DNA molecules into dense core-shell architectures [27]. Notably, DNA loading was accompanied by a modest but statistically significant decrease in zeta potential, from approximately –11.66 mV to –14.19 mV (Figure 1K). This shift toward a more negative surface charge is consistent with partial exposure of the anionic DNA payload at the particle periphery and a corresponding redistribution of cationic lipids toward the nanoparticle core during nucleic acid compaction. The polydispersity index (PDI) remained unchanged and consistently below 0.15, indicating that the particle population remains monodisperse—a prerequisite for reproducible *in vivo* performance (Figure 1K).

Collectively, the comprehensive characterization presented in Figure 1 establishes the successful construction of the DNA^{HcNPV}@LNP-CPP-SORT platform: the C105Y peptide is covalently anchored to the LNP surface, the viral genomic DNA is efficiently encapsulated within the lipid core, and the resulting nanoparticles possess an appropriate size, narrow size distribution, and moderate surface charge. This material foundation sets the stage for the subsequent evaluation of cellular uptake, *in vivo* delivery, and therapeutic efficacy.

2.2 Cellular penetration, cytotoxicity, and mechanistic basis of CPP-SORT synergy

Having confirmed the successful construction of the DNA^{HcNPV}@LNP-CPP-SORT platform, we turned to the question of intracellular delivery and the mechanistic basis for its enhanced activity. Two insect cell lines were selected for this purpose. The first, Sf9, is derived from the fall armyworm *Spodoptera frugiperda*, a species that HcNPV cannot naturally infect; this makes Sf9 cells a stringent model for evaluating delivery that is independent of any native viral entry pathway. The second, S2, originates from *Drosophila melanogaster*, an evolutionarily distant dipteran. Because neither cell line supports productive HcNPV entry through its own envelope proteins, any observed intracellular delivery can be attributed solely to the action of the CPP-SORT module, allowing us to probe its efficiency in isolation.

Scanning electron microscopy (SEM) revealed a striking dichotomy in the interaction of the various formulations with the plasma membrane of both Sf9 and S2 cells. Untreated control cells and those exposed to natural HcNPV displayed smooth, intact surfaces with no discernible topographical abnormalities. In stark contrast, cells incubated with the DNA^{HcNPV}@LNP-CPP-SORT formulation (denoted MAT) exhibited numerous crater-like perforations and membrane discontinuities, with nanocarrier particles visibly embedded or anchored at the breach points (Figure 2A). This direct visual evidence of membrane perturbation is consistent with the proposed dual mechanism of CPP-mediated translocation and SORT-facilitated fusogenic activity, which collectively compromise membrane integrity to facilitate intracellular entry.

To quantify the differential accumulation of nanocarriers on the cell surface, we performed manual counting of particles within randomly selected 5 μm^2 regions of interest positioned either directly over cells (on-cells) or in adjacent cell-free areas (off-cells). In both S2 and Sf9 cultures, particle counts within on-cell regions were significantly elevated for the MAT formulation compared to off-cell backgrounds (Figure 2B). Notably, the magnitude of on-cell particle accumulation was comparable between the two cell lines, suggesting that the CPP-SORT platform engages membrane targets that are broadly conserved across insect species, rather than relying on cell-type-specific receptors. This quantitative metric, derived from direct ultrastructural observation, confirms that the LNP-CPP-SORT platform actively drives membrane engagement and cellular entry, overcoming the intrinsic barriers that restrict passive uptake of naked viral nucleic acids. This differential accumulation confirms that the LNP-CPP-SORT vehicle actively drives cellular association and uptake, circumventing the receptor-mediated restriction that limits native baculovirus infection.

Flow cytometric analysis of cell cycle progression provided the first functional evidence that the internalized viral DNA is not merely present within cells but is transcriptionally active and capable of disrupting host cell cycle regulation (Figure 2C). S2 cells treated with the MAT formulation at 600 ng/mL exhibited pronounced accumulation in the G1 and S phases, indicating a blockage prior to G2 entry. In Sf9 cells, the MAT treatment shifted the distribution toward the S and G2 phases, a pattern consistent with the canonical S/G2 arrest widely documented for baculovirus infections and thought to reflect viral interference with host checkpoint machinery to facilitate genome replication [28]. This cell-type-dependent divergence in arrest phenotype is informative: it suggests that the delivered DNA engages the host cell cycle apparatus differently depending on the cellular context, yet in both cases produces a clear disruption of normal progression. A dose-dependent perturbation of cell cycle distribution was observed across the tested concentration range (100~600 ng/mL) in both lines, with higher doses eliciting progressively greater deviations from the control profiles. Collectively, these data establish that the LNP-CPP-SORT-delivered viral DNA retains full biological competence once internalized, initiating a cytopathic program that, while not identical between cell types, converges on the disruption of host cell cycle progression even in cells that lack the native viral entry machinery.

The dose–response relationship of the MAT formulation was quantified via cell viability assays, yielding half-maximal inhibitory concentrations (IC_{50}) of 542.7 ng/mL for S2 cells and 323.5 ng/mL for Sf9 cells

(Figure 2D). The enhanced sensitivity of Sf9 cells may reflect species-specific differences in endocytic trafficking or intracellular DNA-sensing machinery. Flow cytometric apoptosis analysis further dissected the mode of cell death (Figure 2E–H). In S2 cells, treatment triggered a significant dose-dependent increase in early apoptotic cells (Q3 quadrant), rising from near-baseline levels to approximately 20% at the highest dose tested. Late apoptotic and necrotic populations (Q2 quadrant) expanded in parallel, reaching up to approximately 40%, whereas mechanical damage (Q1 quadrant) remained negligible under all conditions. Viable cells (Q4 quadrant) decreased to approximately 40% at 300 ng/mL, in stark contrast to untreated and native HcNPV controls, where nearly 100% of cells remained viable. A qualitatively similar apoptotic response was observed in Sf9 cells, although the overall magnitude was somewhat attenuated relative to S2 cells. In this line, combined early and late apoptotic populations exceeded 50% of total cells, and the viable fraction dropped to approximately 50%, compared with near-complete viability in control and HcNPV treatments. Native HcNPV virions elicited no detectable apoptotic signal above background in either cell line, reinforcing the conclusion that the LNP-CPP-SORT vehicle is an indispensable prerequisite for the biological activity of the delivered DNA.

To probe the intracellular stress pathways activated by our formulation, we measured reactive oxygen species (ROS) production (Figure 2I–K). Fluorescence microscopy revealed a robust ROS burst in both S2 and Sf9 cells following MAT treatment, whereas untreated controls and native HcNPV-exposed cells showed negligible signal (Figure 2I). Across the tested concentration range (75, 150, and 300 ng/mL), the MAT formulation elevated mean FL3 intensity to approximately 15,000 in S2 cells and 30,000 in Sf9 cells, compared with near-background levels in controls (Figure 2J–K). Notably, in Sf9 cells, the highest MAT concentration (300 ng/mL) elicited a lower ROS signal than the intermediate dose, a pattern not observed in S2 cells. This attenuation at high dose likely reflects rapid progression of Sf9 cells into late-stage apoptosis, at which point extensive mitochondrial collapse curtails further ROS production. Native HcNPV virions generated no detectable ROS response, consistent with their inability to engage intracellular stress pathways in non-host cells. The oxidative burst likely originates from at least two convergent processes: mitochondrial dysfunction associated with viral gene expression and apoptotic onset, and localized membrane destabilization during endosomal escape, where DOTAP-mediated fusogenic activity can directly trigger ROS generation at the endosomal membrane.

To further characterize the intracellular consequences of CPP-SORT-mediated DNA delivery, we assessed mitochondrial membrane potential ($\Delta\Psi m$) using the dual-emission fluorescent probe JC-1. In healthy cells, JC-1 accumulates within intact mitochondria and forms red-fluorescent J-aggregates (detected in the CY3 channel). Upon mitochondrial membrane depolarization, an early and irreversible event in the apoptotic cascade, the probe is released as green-fluorescent monomers (detected in the EGFP channel). Treatment with the MAT formulation elicited a pronounced EGFP signal in both S2 and Sf9 cells, whereas untreated controls and native HcNPV-exposed cells showed negligible green fluorescence (Figure 2L). In S2 cells, the MAT-induced EGFP intensity exceeded that of the positive control by more than two-fold, indicating severe mitochondrial dysfunction. Mean EGFP fluorescence values ranged from approximately 15,000 to 30,000 across all tested MAT concentrations, compared with fewer than 5,000 in CK and HcNPV groups (Figure 2M). The comparable level of depolarization

observed across the entire MAT dose range suggests that even the lowest concentration tested suffices to saturate the mitochondrial damage response in these non-host cell systems. Native HcNPV virions, by contrast, displayed EGFP fluorescence indistinguishable from untreated controls, confirming that intact virions are unable to engage the mitochondrial apoptotic machinery under these conditions. Collectively, these results demonstrate that the LNP-CPP-SORT-delivered viral DNA, but not the native virion, triggers mitochondrial membrane depolarization, a key initiating event in the intrinsic apoptotic cascade. This finding provides a direct mechanistic link between the intracellular delivery of viral DNA and the apoptotic cell death documented in the preceding sections.

Collectively, the data presented in Figure 2 establish a coherent mechanistic narrative. The DNA^{HcNPV}@LNP-CPP-SORT platform achieves robust cellular association and membrane penetration in non-host insect cells, culminating in the formation of crater-like perforations and extensive particle accumulation on the cell surface, phenomena that native HcNPV virions fail to elicit. Once internalized, the delivered viral DNA proves transcriptionally active and biologically competent, triggering the full repertoire of baculovirus cytopathology: cell cycle arrest at G1/S in S2 cells and S/G2 in Sf9 cells, mitochondrial membrane depolarization, reactive oxygen species production, and ultimately apoptotic cell death. The CPP moiety drives the initial adhesion and membrane translocation steps, physically breaching the plasma membrane barrier [29], while the SORT molecule DOTAP facilitates endosomal escape and intracellular trafficking, enabling the DNA payload to reach the cytoplasm and engage host transcriptional machinery [30]. This dual-functional synergy transforms a viral genome that is otherwise inert when delivered as an intact virion into a potent intracellular toxin in non-host cells, providing the mechanistic foundation for the enhanced *in vivo* efficacy documented in the subsequent figures.

2.3 Bridging scales: from cellular mechanism to field-level control

Having established that the DNA^{HcNPV}@LNP-CPP-SORT platform achieves robust intracellular delivery in cultured insect cells, we next asked whether this performance translates into meaningful gains at the organismal level and, ultimately, under field conditions. The true measure of an agricultural nanocarrier lies not in its behavior under the controlled environment of a cell culture dish, but in its capacity to function within the complex physiological milieu of the living insect and across the variable and often harsh conditions of on-site application. To address this, we conducted a comprehensive series of *in vivo* experiments spanning multiple biological scales: histopathological analysis of midgut tissue, quantitative viral gene expression profiling, controlled laboratory bioassays, and replicated field trials conducted across two independent growing seasons at geographically distant locations.

The midgut epithelium is the primary site of baculovirus entry and the principal barrier that must be breached for systemic infection to proceed. We hypothesized that the enhanced intracellular delivery conferred by the CPP-SORT synergy would manifest histologically as accelerated tissue-level pathology. *H. cunea* larvae were orally administered either native HcNPV or the DNA^{HcNPV}@LNP-CPP-SORT formulation, and midgut tissues were harvested at 24 h post-treatment for histological staining (Figure 3A). Larvae treated with CK or native HcNPV displayed relatively intact midgut architecture: the columnar

epithelial cells remained largely adherent to the basement membrane, the brush border was discernible, and the peritrophic matrix maintained structural coherence. In stark contrast, the MAT formulation induced widespread destruction of the peritrophic matrix and extensive sloughing of the midgut epithelium, evident as a markedly reduced epithelial layer compared with both CK and HcNPV groups (Figure 3A). This accelerated tissue-level pathology provides direct histological evidence that our platform not only delivers viral DNA into cultured cells but also expedites the critical process of gut barrier traversal, an essential prerequisite for lethal infection by orally acquired entomopathogens.

Quantitative viral gene expression confirms accelerated onset of the viral replication program. To obtain quantitative molecular confirmation of the histopathology findings, we profiled the expression of six canonical HcNPV genes spanning the full temporal cascade—immediate-early (*ie1*, *pe38*), early/late (*lef8*), late (*vp39*, *p10*), and very late (*polh*)—in midgut tissue 24 and 48 h post-treatment using quantitative real-time PCR (Figure 3B). At 24 h, the DNA^{HcNPV}@LNP-CPP-SORT formulation elicited a dramatic and selective induction of immediate-early gene expression: *ie1* and *pe38* transcript levels were approximately 10~20-fold higher than those measured in native HcNPV-treated larvae. This pronounced early transcriptional burst indicates that the nanocarrier-delivered DNA bypasses the rate-limiting steps of virion disassembly and nuclear import that constrain native infection, allowing the viral genome to engage host transcriptional machinery almost immediately upon delivery. Transcripts of *lef8*, *vp39*, and *p10*—markers of viral DNA replication, capsid assembly, and cell lysis, respectively—were also significantly elevated at approximately 5-fold over native HcNPV levels, confirming that the transcriptional program progressed efficiently from early to late phases. In contrast, *polh*, a very late gene encoding the polyhedrin matrix protein, was not induced above control levels at 24 h in either treatment, consistent with its expected expression later in the infection cycle. By 48 h, transcript levels of most genes had converged between the MAT and native HcNPV groups, indicating that both treatments ultimately support a comparable viral replication program once the native virus completes its delayed entry. Notably, however, *p10* remained 2.5-fold higher in MAT-treated larvae and was the only gene for which the difference remained statistically significant at this time point, implying that the MAT formulation sustains a heightened level of cell lysis and virion release beyond the acute infection phase. This transcriptional profile suggests that the LNP-CPP-SORT platform does not merely deliver DNA more efficiently. Rather, it fundamentally accelerates the kinetics of viral gene expression, compressing the timeline from initial exposure to productive infection.

A persistent criticism of baculovirus biopesticides is their slow speed of kill, which allows larvae to continue feeding and incurring economic damage for days after application. We therefore conducted controlled indoor bioassays to quantify whether the DNA^{HcNPV}@LNP-CPP-SORT formulation could meaningfully shorten the time to mortality relative to native HcNPV (Figure 3C). Second-instar *H. cunea* larvae were fed leaf discs treated with equivalent doses of either formulation, and mortality was recorded daily for 14 days. The difference in early-phase mortality was unequivocal: the first dead larvae appeared in the MAT group at 2 days post-application, compared with 4 days for native HcNPV, and by day 4 cumulative mortality in the MAT group had reached a significantly higher level (Figure 3C). Beyond

this early window, mortality in the two treatment groups progressed in parallel and ultimately converged to comparable final levels by day 14. This temporal pattern carries two important implications. First, the early-phase superiority of the MAT formulation aligns precisely with the accelerated tissue pathology and amplified immediate-early viral gene expression documented above, establishing a coherent chain of causality from molecular mechanism to organismal outcome. Second, the convergence of final mortality indicates that the intrinsic virulence ceiling is dictated by the viral genome itself, not by the delivery platform. In other words, the LNP-CPP-SORT system accelerates the onset of lethal infection without altering its ultimate outcome, a property that constitutes a predictable and therefore biologically safe mode of enhancement.

Field trial I: single-application efficacy under operational conditions. Translating laboratory efficacy to field performance is the decisive hurdle for any agricultural nanocarrier. We evaluated the DNA^{HcNPV}@LNP-CPP-SORT formulation in two independent field trials; the first employed a single application to assess efficacy under a conservative spray regime. Larval population counts in the MAT-treated plots were consistently lower than those in CK and native HcNPV groups throughout the monitoring period, with significant reductions observed from day 12 onward and a final larval reduction rate of 77.9%, compared with 53.7% for native HcNPV and 5.4% for the untreated control (Figure 3D). The corrected control efficacy of the MAT formulation surpassed that of native HcNPV beginning at day 8 and remained significantly higher through the trial endpoint (Figure 3E). This early separation—achieved with a single spray—is practically meaningful: it demonstrates that the accelerated speed of action observed in laboratory bioassays translates into faster pest suppression under field conditions, a critical advantage when rapid knockdown is required to curtail feeding damage.

To assess the robustness of the formulation under variable environmental conditions, we examined the relationship between local meteorological factors and control efficacy across the trial period. The MAT formulation maintained superior performance regardless of fluctuations in temperature or wind force (Figure 3F). Regression analysis identified the number of days post-application as the only significant predictor of efficacy for both the MAT and native HcNPV treatments, indicating that the materials performed consistently across the range of weather conditions encountered. Finally, we performed a lag-day correlation analysis to probe the temporal relationship between temperature and efficacy. The strongest correlation coefficient was observed at a 5-day lag, with values of 0.69 for MAT and 0.75 for native HcNPV (Figure 3G). The near-identical lag structure between the two treatments reinforces a conclusion that has emerged repeatedly throughout this study: the MAT platform accelerates the onset of lethal infection but does not alter the intrinsic temperature dependence of the virus, which ultimately governs the rate of disease progression in the field.

Field trial II: two-application regimen confirms consistency across variable conditions. The second field trial employed two sequential applications spaced 6 days apart, with an overall trial duration of 15 days. Despite differences in spray regimen and ambient environmental conditions, the outcome was remarkably consistent with that of the first trial. Larval counts in the MAT-treated plots were significantly lower than those in the native HcNPV group at day 9 and remained so from day 12 through day 15

(Figure 3H). The temporal trajectory of corrected control efficacy mirrored this pattern: the MAT formulation achieved significantly higher efficacy from day 9 onward, with the advantage sustained through the trial endpoint (Figure 3I). Larval activity levels did not differ significantly between treatments throughout the monitoring period (Figure 3J), suggesting that the observed differences in population reduction stem from differential mortality rather than from altered feeding or dispersal behavior. Notably, larval activity was negatively correlated with control efficacy in both MAT and native HcNPV treatments, whereas no significant association was found with ambient temperature (Figure 3K), reinforcing the conclusion that treatment-driven mortality, rather than passive climatic effects, was the primary determinant of pest suppression.

Lag-day analysis of the relationship between temperature and efficacy revealed two distinct peaks: a correlation maximum at 3–4 days and 7 days for the first application (Figure 3L), yielding coefficients of 0.51 and 0.57, respectively. This biphasic lag structure echoes the pattern observed in Trial I and is consistent with the known temperature-dependent kinetics of baculovirus replication, wherein warmer conditions accelerate disease progression within a characteristic temporal window post-exposure. The reproducibility of this lag structure across independent trials, spray regimens, and growing seasons underscores a central theme of this study: the DNA^{HcNPV}@LNP-CPP-SORT platform accelerates the onset of infection without overriding the intrinsic thermal biology of the virus itself.

The data presented in Figure 3 span more than six orders of biological scale, yet they converge on a single coherent conclusion. At the molecular level, the LNP-CPP-SORT platform triggers an immediate-early transcriptional burst (*ie1* and *pe38* upregulated approximately 20-fold within 24 h) that compresses the timeline from DNA delivery to viral gene expression. At the tissue level, this molecular acceleration manifests as catastrophic midgut epithelial disruption that occurs substantially earlier than with native HcNPV. At the organismal level, the accelerated pathology translates into a markedly shortened time to mortality under controlled conditions, without altering the final mortality ceiling, which is dictated by the viral genome itself. At the population level, two independent field trials, conducted across different growing seasons, spray regimens, and geographic locations, consistently demonstrate significant improvements in both larval population reduction and corrected control efficacy relative to native HcNPV. Notably, the near-identical lag-day structures between MAT and native HcNPV treatments, reproduced across both trials, indicate that the platform accelerates the kinetics of infection without overriding the intrinsic temperature dependence of the virus.

This multi-scale concordance validates the central hypothesis of this study: the dual-functional CPP-SORT design, engineered to overcome the sequential barriers of peritrophic matrix penetration and endosomal escape, confers a genuine kinetic advantage to the delivered viral DNA payload. The platform does not merely protect DNA from environmental degradation; it actively facilitates its journey from the gut lumen to the host cell nucleus, compressing the timeline from exposure to productive infection and thereby addressing the slow speed of kill that has historically constrained baculovirus biopesticides. Equally important, the convergence of final mortality between MAT and native HcNPV, together with the preserved thermal response profile, establishes a predictable and therefore biologically safe mode of

enhancement, one that accelerates disease progression without introducing novel virulence characteristics. Collectively, these findings establish the DNA^{HcNPV}@LNP-CPP-SORT platform as a field-ready precision biocontrol agent and provide a mechanistic blueprint for the rational design of nanocarriers that function across the formidable physiological barriers of the insect gut.

2.4 Potency without compromise: environmental stability and species selectivity

A defining vulnerability of nucleic acid-based biopesticides is their rapid inactivation under field-relevant environmental conditions, a limitation that has historically restricted their use to narrow application windows and favorable weather [12, 31, 32]. The DNA^{HcNPV}@LNP-CPP-SORT platform was designed to confront this challenge directly. Its lipid bilayer is not a passive envelope but a functional barrier that physically sequesters the DNA payload, insulating it from the UV radiation, thermal fluctuations, and nucleolytic enzymes that would otherwise destroy it before ingestion by the target larva. Yet potency alone is an insufficient metric for an agricultural nanocarrier. Any particle deployed at field scale must also demonstrate a benign safety profile toward the broader ecosystem within which it operates [33]. These two requirements of enhanced environmental persistence and ecological selectivity are often in tension: modifications that improve the former risk compromising the latter. In this section, we systematically evaluate whether a single, rationally designed platform can satisfy both criteria simultaneously. To do so, we assess environmental stability under a panel of abiotic stressors, and we probe ecological safety across three complementary non-target models: a non-target lepidopteran herbivore (*Spodoptera frugiperda*), a beneficial predatory insect (*Coccinella septempunctata*), and a vertebrate aquatic organism (*Danio rerio*). This multi-species framework provides an integrated assessment of the platform's suitability for operational deployment.

We first examined the physical appearance and macroscopic integrity of the formulation following exposure to three representative environmental stressors: elevated temperature (42°C), ultraviolet C (UVC) irradiation (253.7 nm), and natural outdoor conditions combining full-spectrum solar radiation with ambient summer temperatures. Visual inspection after 6, 12, and 24 h of exposure revealed that native HcNPV solutions subjected to outdoor conditions developed visible turbidity and particulate matter within 6 h, consistent with nucleic acid aggregation and/or denaturation (Figure 4A). The DNA^{HcNPV}@LNP-CPP-SORT formulation (denoted MAT), by comparison, remained optically transparent and macroscopically homogeneous across all time points and stress conditions, indicating that lipid encapsulation preserves colloidal stability and shields the encapsulated DNA from environmentally induced aggregation.

To quantify the protective efficacy at the molecular level, we extracted nucleic acids from stressed samples and measured the residual concentration of HcNPV genomic DNA. Naked DNA was undetectable within 1 h of exposure to all three stress conditions. The MAT formulation preserved detectable DNA levels throughout the full 24 h monitoring period, although its protective capacity remained inferior to that of the native polyhedrin shell of HcNPV, which sequesters viral DNA within a crystalline protein matrix and confers substantial environmental resilience (Figure 4B). To further verify

DNA integrity, we PCR-amplified the *pe38* gene from stressed samples. Successful amplification requires an intact template and unimpeded access of the polymerase to the target sequence. Accordingly, *pe38* was readily amplified from both native HcNPV and demulsified MAT but not from intact MAT, confirming that the lipid bilayer physically occludes the encapsulated DNA from external molecular probes. Direct comparison of *pe38* band intensities across treatments revealed that the MAT formulation produced visibly stronger amplicons than naked DNA after 24 h of stress exposure across all three stress conditions (Figure 4C). In repeated quantitative assessments, the MAT formulation retained significantly higher DNA concentrations than unprotected DNA at the 24 h endpoint under all three stress regimens. This protection translated into an effect size (MAT minus naked DNA) of 58.53 to 73.42 ng/μL across conditions, with the largest differential observed under UVC irradiation (Figure 4D). These values represent a substantial reservoir of intact genetic material that would otherwise be lost to environmental degradation before the virus could reach its target.

DNA preservation, while necessary, does not guarantee that the formulation retains its biological potency after stress exposure. We therefore subjected stressed MAT formulations to both S2 and Sf9 cells and quantified the resulting cytotoxic activity (Figure 4E–I). Cell counts were obtained using two complementary image-based methods, each tailored to the distinct morphology of the respective cell line: an automated blob-detection pipeline for the small, uniform S2 cells, and a supervised regression approach trained on manually annotated regions of interest for the irregularly shaped Sf9 cells. Both methods were independently validated and produced consistent estimates across replicates (see Methods and Data S1–S2 for details).

In S2 cells, neither naked DNA nor native HcNPV virions induced detectable cytotoxicity under any of the stress conditions tested, consistent with their inability to engage intracellular targets in this non-host cell line (Figure 4G). The behavior of the MAT formulation depended strongly on the nature of the stress. Following exposure to elevated temperature (42 °C), MAT largely lost its cytotoxic activity: at all three time points examined (1, 6, and 12 h) and across the full dose range (75, 150, and 300 ng/mL), the viable cell fraction remained no less than that of untreated controls. This result stands in apparent contrast to the DNA protection data presented above, which showed that MAT effectively shields the encapsulated DNA from thermal degradation. The discrepancy can be rationalized, however, by considering the distinct damage mechanisms at play. High temperature primarily denatures unprotected nucleic acids through direct thermal destabilization of the double helix, a process that the lipid bilayer can effectively counteract by physical sequestration. Yet elevated temperature may simultaneously compromise the functional integrity of the nanoparticle itself. For instance, by altering lipid phase behavior, disrupting the surface presentation of CPP ligands, or promoting particle aggregation at the membrane interface, thereby impairing cellular uptake even though the DNA cargo remains intact. In contrast, MAT formulations subjected to UVC and outdoor exposure largely retained their cytotoxic activity. Following UVC treatment, significant cell killing was observed after both 6 and 12 h of pre-exposure, while outdoor-treated MAT required a longer stress duration (12 h) to achieve comparable efficacy (Figure 4G). This pattern indicates that the LNP-CPP-SORT platform is more resilient to photochemical damage than to thermal stress, an advantage likely attributable to the fact that UV-induced damage primarily targets the

nucleic acid payload—which the lipid bilayer effectively shields—whereas thermal stress compromises the delivery vehicle itself.

For Sf9 cells, cell counts were obtained using a supervised Ridge regression model trained on manually annotated regions of interest, which produced estimates in close agreement with manual counts and provided a reliable basis for downstream comparisons (Figure 4H; see Methods for details). The same as observed in S2 cells, neither naked DNA nor native HcNPV virions exhibited detectable cytotoxicity to Sf9 under any stress condition (Figure 4I). The MAT formulation, however, significantly reduced Sf9 cell numbers following outdoor exposure at both 6 and 12 h, an effect that was evident across all three tested concentrations. UVC-treated MAT similarly retained its cytotoxic capacity, producing significant cell depletion after 6, 12, and 24 h of pre-exposure across the full dose range. These results mirror the pattern observed in S2 cells and reinforce the conclusion that the LNP-CPP-SORT platform is more resilient to photochemical damage than to thermal stress: UV radiation primarily threatens the nucleic acid payload, which the lipid bilayer effectively shields, whereas elevated temperature appears to compromise the functional integrity of the delivery vehicle itself, even when the DNA cargo remains intact.

Flow cytometric analysis of cell state distribution provided a more detailed view of the cytotoxic response elicited by stressed MAT formulations (Figure 4J–K). In S2 cells, untreated controls and those exposed to naked DNA or native HcNPV maintained a predominantly intact cell population across all conditions. The MAT formulation, by contrast, produced marked shifts in cell state distribution. Notably, following exposure to 42 °C for as little as 1 h, MAT induced significant increases in early apoptosis, late apoptosis, and mechanical damage across all three tested dosages, with the effect persisting at selected doses after 6 and 12 h of thermal stress. This rapid onset of damage under thermal stress is consistent with the interpretation advanced earlier: elevated temperature, while sparing the DNA payload, likely compromises the functional integrity of the nanoparticle surface, and the resulting partially damaged particles may still be capable of engaging and disrupting the plasma membrane upon contact with cells. For UVC condition, MAT significantly elevated apoptotic populations across all exposure durations (1, 6, and 12 h) and across the full dose range (75–300 ng/mL), mirroring the pattern observed in the cytotoxicity assays (Figure 4K). In Sf9 cells, however, the same stressed MAT formulations failed to elicit any detectable shift in cell state distribution, with all populations remaining indistinguishable from those of untreated controls (Figure S1). This striking cell-line-dependent difference mirrors the attenuated apoptotic response of Sf9 cells documented earlier (Figure 2F–H) and may reflect intrinsic differences between the two lines in membrane composition, endocytic capacity, or stress-response thresholds that collectively modulate susceptibility to nanoparticle-mediated damage. Importantly, the complete absence of a response in Sf9 cells, rather than a partial or variable effect, suggests a qualitative rather than merely quantitative difference in how these two insect cell lines interact with the LNP-CPP-SORT platform.

A central premise of our platform design is that the delivery enhancement conferred by CPP-SORT synergy should manifest only in hosts whose midgut environment supports CPP-mediated translocation

and SORT-facilitated endosomal escape. To test this prediction, and to critically evaluate the ecological safety of the formulation, we conducted oral toxicity bioassays in three complementary non-target models. We begin here with the fall armyworm, *Spodoptera frugiperda*, a lepidopteran species that HcNPV cannot naturally infect. Larvae were fed leaf discs treated with native HcNPV or the MAT formulation, and survival and pupation were monitored over 7 days. The survival curves of the two treatments were superimposable, and cumulative mortality remained indistinguishable from that of untreated controls (Figure 4L). Pupation rates likewise did not differ among the three groups. These results demonstrate that the MAT formulation does not confer a promiscuous gain-of-function; rather, CPP-SORT enhancement is context-dependent and requires the specific host environment to manifest. That the formulation fails to potentiate HcNPV DNA toxicity in *S. frugiperda*, a species that shares broad gut physiological features with the target host, underscores the exquisite selectivity of this platform and its minimal risk of off-target effects on non-target pests.

We further extended the safety evaluation to compare two distinct CPP ligands, C105Y and PAR, each formulated into the MAT platform and tested at low, medium, and high doses alongside CK and native HcNPV controls. The assessment spanned all three non-target models: fall armyworm, ladybug, and zebrafish (Figure 4M–O). Across all three species, survival rates remained uniformly high and did not differ significantly among treatments, regardless of CPP identity or dose. The highest mortality was observed in ladybug, with a maximum of 4 deaths out of 10 individuals over the 6-day observation period, but this level was statistically indistinguishable from that recorded in CK and native HcNPV groups (Figure 4N). Fall armyworm exhibited even lower mortality, with no more than 2 deaths per 10 individuals across all treatments (Figure 4M). Zebrafish, tested in an aqueous exposure format, showed the lowest overall mortality, with a maximum of 3 deaths per 30 individuals over 5 days (Figure 4O). Necropsy examination of zebrafish revealed no observable morphological abnormalities across any treatment group. The gross appearance of the liver, including tissue texture and color, remained indistinguishable from that of untreated controls, indicating the absence of visible pathological changes by MAT in this primary detoxification organ (Figure 4P). The consistently high survival across three phylogenetically and ecologically distinct organisms, combined with the absence of any dose-response relationship for either CPP variant, argues strongly that the LNP-CPP-SORT platform is inherently benign toward non-target species. Moreover, the equivalent safety profiles of C105Y- and PAR-functionalized formulations suggest that the selectivity of the platform is a general feature of the dual-ligand design, rather than an artifact of a particular peptide sequence. From an ecological standpoint, the preservation of ladybug survival is especially noteworthy, as this predatory species occupies the same trophic niche as the target pest and would be among the first organisms exposed to any field-applied formulation.

2.5 Summary and perspective: A clinically inspired platform for precision pest management

The data presented in this study span more than six orders of biological scale from subcellular gene expression to landscape-level pest suppression, and they converge on a single coherent conclusion. At the molecular level, the LNP-CPP-SORT platform triggers an immediate-early transcriptional burst that compresses the timeline from DNA delivery to viral gene expression. At the tissue level, this molecular

acceleration manifests as catastrophic midgut epithelial disruption that occurs substantially earlier than with native HcNPV. At the organismal level, the accelerated pathology translates into a markedly shortened time to mortality under controlled conditions, without altering the final mortality ceiling dictated by the viral genome itself. At the population level, two independent field trials, conducted across different growing seasons, spray regimens, and geographic locations, consistently demonstrate significant improvements in both larval population reduction and corrected control efficacy. The near-identical lag-day structures between MAT and native HcNPV treatments, reproduced across both trials, further indicate that the platform accelerates the kinetics of infection without overriding the intrinsic temperature dependence of the virus. Collectively, these multi-scale findings validate the central hypothesis of this study: the dual-functional CPP-SORT design, engineered to overcome the sequential barriers of peritrophic matrix penetration and endosomal escape, confers a genuine kinetic advantage to the delivered viral DNA payload, compressing the timeline from exposure to productive infection and thereby addressing the slow speed of kill that has historically constrained baculovirus biopesticides.

Beyond efficacy, a successful agricultural nanocarrier must also withstand the abiotic stressors encountered during field application and demonstrate a benign safety profile toward non-target organisms. The DNA^{HcNPV}@LNP-CPP-SORT platform meets both requirements. Its lipid bilayer physically sequesters the DNA payload, preserving colloidal stability and protecting the encapsulated genome from UV radiation, thermal fluctuations, and nucleolytic degradation under conditions that rapidly destroy naked viral DNA. This environmental resilience translates directly into retained biological potency: stressed MAT formulations maintain their full cytotoxic and apoptosis-inducing capacity even after prolonged exposure to UVC and natural outdoor conditions. Equally important, the platform exhibits remarkable species selectivity. Oral toxicity bioassays across three complementary non-target models revealed no detectable mortality or sublethal developmental impairment, regardless of CPP variant or dose. The inability of the formulation to potentiate HcNPV DNA toxicity in Spodoptera frugiperda, a species that shares broad gut physiological features with the target host, underscores the exquisite selectivity conferred by the context-dependent action of the CPP-SORT machinery. That ladybug survival and zebrafish development were entirely unaffected further reinforces the conclusion that this platform is inherently benign toward organisms occupying different ecological niches.

The findings presented here establish the DNA^{HcNPV}@LNP-CPP-SORT platform as a field-ready precision biocontrol agent that simultaneously achieves three critical benchmarks: accelerated speed of kill, robust environmental persistence, and a favorable ecological safety profile characterized by species-selective enhancement. More broadly, it shows that clinical nanomaterials can be engineered for variant targets, moving beyond their original medical scope [34]. As recently articulated in the field [22], peptide-based materials represent a key frontier for next-generation nucleic acid delivery, and our CPP-functionalized SORT-LNP platform provides an early demonstration of this paradigm in a non-mammalian system. It provides a mechanistic blueprint that is, in principle, adaptable to other insect-virus systems and, potentially, to other nucleic acid cargoes [35]. The successful extension of this platform to two distinct CPP sequences and its compatibility with diverse environmental conditions

further suggest that the approach is robust and generalizable. As global agriculture faces mounting pressure to reduce reliance on broad-spectrum chemical insecticides, precision nanomedicine strategies of the kind exemplified here offer a promising route toward sustainable, ecologically responsible pest control [36].

3 Materials and Methods

3.1 Materials and reagents

The *H. cunea* laboratory colony was originally established from individuals obtained from a maintained laboratory population at Hebei University (Hebei, China), which originally collected from Shanghe, Shandong Province (37.33° N, 116.88° E), and was reared on fresh mulberry leaves. Fall armyworm larvae were reared on an artificial diet and had been maintained as a continuous laboratory culture, originally collected from Dali, Yunnan (25.96° N, 100.40° E). Adults of the ladybug *Coccinella septempunctata* were collected from Dali, Yunnan (25.34° N, 100.49° E) and kept under laboratory conditions until use. Zebrafish (*Danio rerio*, wildtype AB) were obtained from a domestic commercial supplier (Zebrafish Model Animal Research Center, Shanghai, China). All insect rearing was conducted at 25 ± 2 °C, 60% relative humidity, and a 16:8 h light-dark photoperiod. Zebrafish were maintained at 28.5 ± 0.5°C under the photoperiod of 14 L : 10 D. Key biological materials and reagents used in this study were provided in Table 1.

The HcNPV isolate was propagated in third-instar *H. cunea* larvae by feeding them mulberry leaves coated with a viral suspension (1×10^7 PIBs/mL). Cadavers displaying typical NPV symptoms were collected from day 5 onward, kept at room temperature for 2 days to allow liquefaction, and stored at -20°C. For purification, cadavers were homogenized in PBS, filtered through gauze, and subjected to differential centrifugation (500 × g for 10 min, then 4,500 × g for 30 min at 4°C). The resulting pellet was resuspended and further purified by sucrose density gradient ultracentrifugation (30%, 45%, 60% sucrose) at 3,000 × g for 25 min. The opaque band at the 45%–60% interface was collected, washed repeatedly with sterile water (10,000 × g, 30 min), and freeze-dried to obtain HcNPV powder, which was stored at -20°C until further use.

3.2 Synthesis of DSPE-PEG_{2000}-CPP conjugates

C105Y peptide (10 mg) and an equimolar amount of DSPE-PEG_{2000}-Mal were dissolved in 3 mL of anhydrous DMF containing DIEA as a catalyst. The mixture was stirred under nitrogen at 250 rpm for 2 h in an ice bath protected from light. The pH was then adjusted to 7.4. The reaction mixture was transferred to a dialysis membrane (MWCO 3500 Da) and dialyzed against 2 L of deionized water for 24 h, followed by an additional 24 h of dialysis against fresh deionized water. The dialysate was lyophilized to obtain DSPE-PEG_{2000}-C105Y as a white powder, which was stored at -20°C until use. DSPE-PEG_{2000}-PAR was synthesized analogously, using DSPE-PEG_{2000}-NHS and the PAR peptide under standard NHS-

amine coupling conditions (DMF, DIEA, N_2, room temperature), followed by dialysis purification and lyophilization.

For ^{1}H NMR analysis, C105Y peptide, DSPE-PEG_{2000}-Mal, and the purified DSPE-PEG_{2000}-C105Y conjugate were each dissolved in D_2O at a concentration of approximately 10 mg/mL and transferred to NMR tubes. ^{1}H NMR spectra were recorded at room temperature on a Bruker Avance III HD NanoBay 400 MHz spectrometer equipped with a 5 mm PABBO BB/ probe. Spectra were acquired using the standard zg30 pulse sequence (16 scans, 1.0 s relaxation delay) and processed with a line broadening of 0.30 Hz. Chemical shifts were referenced to the residual HDO signal at δ 4.79.

For Fourier Transform Infrared (FTIR) spectroscopy, C105Y peptide, DSPE-PEG_{2000}-Mal, and the purified DSPE-PEG_{2000}-C105Y conjugate were each mixed with KBr and thoroughly ground under dry conditions. The mixtures were pressed into transparent pellets and analyzed on a Shimadzu IRTracer-100 FTIR spectrometer over the range of 4000–500 cm^{-1}. Characteristic absorption peaks were recorded and compared to verify the structural features of the conjugate.

3.3 Preparation of DNA^{HcNPV}@LNP-CPP-SORT

The SORT-LNP platform was constructed following established clinical protocols, with the incorporation of DSPE-PEG_{2000}-CPP as a functionalized lipid component [21]. Purified HcNPV occlusion bodies (1 × 10^8 PIBs/mL) were collected by centrifugation at 10,000 × g for 8 min at 4°C. The pellet was resuspended in 0.1 M Na_2CO_3 and incubated at room temperature for 30 min with intermittent mixing to release virions. After neutralization with 1 M Tris-HCl (pH 7.6) to a final concentration of 0.1 M, the suspension was centrifuged at 7,000 × g for 10 min, and the supernatant was collected. Virions were concentrated using the virus concentration kit and then lysed in a buffer containing 10 mM Tris-HCl (pH 7.6), 10 mM EDTA, and 0.25% SDS at 37°C for 1.5 h. Proteinase K was added to a final concentration of 500 μg/mL, and digestion was continued at 37°C for at least 4 h. Genomic DNA was extracted with phenol-chloroform, precipitated with ethanol and sodium acetate, washed with 70% ethanol, and dissolved in ddH_2O. The purified DNA was stored at -20°C until use.

The identity of HcNPV was confirmed by PCR amplification of the *polyhedron* and *pe38* genes (Table S1). Amplification was performed in a 25 μL reaction containing 12.5 μL of 2× Taq Master Mix, 1 μL of each primer (10 μM), and 2 μL of viral genomic DNA template. The thermal cycling program consisted of an initial denaturation at 95°C for 5 min, followed by 35 cycles of 95°C for 30 s, 55°C for 30 s, and 72°C for 45 s, with a final extension at 72°C for 10 min. PCR products were resolved on a 0.8% agarose gel, stained with GelStain, and visualized under a gel imaging system. Bands matching the expected sizes were excised, purified, and sequenced. The obtained sequences were aligned against known HcNPV gene sequences to confirm identity.

Lipid nanoparticles loaded with HcNPV genomic DNA were prepared by the thin-film hydration-extrusion method. Briefly, DLin-MC3-DMA, DSPC, cholesterol, DSPE-PEG_{2000}-CPP, and DOTAP were mixed at a

molar ratio of 25:5:19.3:0.8:50 and dissolved in an ethanol-chloroform mixture (1:2, v/v). The organic solvent was removed by rotary evaporation at 45°C to form a homogeneous lipid film. HcNPV genomic DNA dissolved in nuclease-free water was added to hydrate the lipid film for 40 min at a DNA-to-total-lipid mass ratio of 6:100. The resulting suspension was dispersed by ultrasonication in an ice bath and sequentially extruded through 400 nm and 200 nm polycarbonate membranes (10 passes each) using a liposome extruder. Blank LNP-CPP were prepared by the same procedure omitting the DNA.

3.4 Physicochemical characterization

The particle size and polydispersity index (PDI) of Blank-LNP-CPP and DNA^{HcNPV}@LNP-CPP were determined by dynamic light scattering (DLS) using a Zetasizer Nano ZS-90 (Malvern Instruments, UK). Samples were diluted with ultrapure water and briefly sonicated prior to measurement. Zeta potential was measured on a Zetasizer Nano ZSP (Malvern Instruments, UK) at 25°C after appropriate dilution with ultrapure water, with each sample analyzed in triplicate. For transmission electron microscopy (TEM), the nanoparticle suspensions were ultrasonicated for 5 min, and 10 μL of each sample was deposited onto carbon-coated copper grids. After 5 min of adsorption, excess liquid was removed with filter paper, and the grids were dried under an infrared lamp. Specimens were examined using a HITACHI 7650 transmission electron microscope to evaluate nanoparticle morphology, size, and dispersion state.

3.5 Cell culture

S2 cells, derived from *D. melanogaster* embryos, were maintained in Schneider's *Drosophila* Medium supplemented with 10% heat-inactivated fetal bovine serum and 1% penicillin-streptomycin [37]. Cultures were incubated at 28°C under normal atmospheric conditions without CO_2 enrichment. Sf9 cells, a clonal isolate of the *S. frugiperda* Sf21 cell line originally established from pupal ovarian tissue, were cultured in TNM-FH medium containing 10% heat-inactivated fetal bovine serum and 1% penicillin-streptomycin under the same incubation conditions [38].

3.6 Scanning electron microscopy of cells

S2 and Sf9 cells were seeded onto coverslips and treated with native HcNPV or the DNA^{HcNPV}@LNP-CPP formulation as described above. After treatment, the cells were washed gently with PBS and fixed with 2.5% glutaraldehyde in 0.1 M phosphate buffer (pH 7.4) for 2 h at room temperature, followed by three washes with PBS. The fixed cells were dehydrated through a graded ethanol series (30%, 50%, 70%, 90%, and 100%, 10 min each) and chemically dried using hexamethyldisilazane (HMDS). The coverslips were mounted onto aluminum stubs, sputter-coated with a thin conductive layer of gold, and examined using a field-emission scanning electron microscope (FEI/Thermo Fisher) operated at an accelerating voltage of 5 kV. Images were acquired at magnifications of ×5,000 and ×10,000 using a secondary electron detector.

3.7 Cell cycle analysis

S2 and Sf9 cells were seeded into 6-well plates at a density of 1 × 10^6 cells per well and cultured for 24 h. Cells were then treated with the MAT formulation at final concentrations of low, mid, and high from 100–600 ng/mL, with untreated cells serving as the control. After 12 h of treatment, cells were harvested by gentle pipetting, collected by centrifugation at 1,000 rpm for 5 min, washed once with ice-cold PBS, and fixed in 1 mL of ice-cold 70% ethanol at 4°C for 12–24 h. The fixed cells were centrifuged, resuspended in PBS, and stained with 0.5 mL of propidium iodide (PI) staining solution according to the manufacturer's instructions. Following incubation at 37°C for 30 min in the dark, samples were analyzed by flow cytometry at an excitation wavelength of 488 nm. Data were processed using FlowJo software.

3.8 Cell viability assay

S2 and Sf9 cells in the logarithmic growth phase were seeded into 96-well plates at a density of 2,000 cells per well and cultured for 48 h at 28°C. Cells were then treated with the MAT formulation at final concentrations ranging from 100 to 1000 ng/mL and incubated for 12 and 24 h, respectively. Blank wells containing medium without cells were included as background controls. Cells treated with 6000 ng/mL HcNPV were used as comparison. After treatment, 10 μL of CCK-8 solution was added to each well, and the plates were incubated at 28°C for 1–4 h. The optical density was measured at 450 nm using a microplate reader. Cell viability was calculated as (ODtreatment − ODblank) / (ODcontrol − ODblank) × 100%, and the half-maximal inhibitory concentration (IC_{50}) was determined from the dose-response curve.

3.9 Apoptosis assay

S2 and Sf9 cells in the logarithmic growth phase were seeded into 6-well plates at a density of 1 × 10^6 cells per well and cultured for 24 h. Cells were then treated with the MAT formulation at final concentrations of 75, 150, and 300 ng/mL, with untreated or HcNPV treated cells serving as the control. After 12 h of treatment, the culture medium was collected, and the adherent cells were washed with PBS, harvested by trypsinization, and combined with the culture medium. The cell suspension was centrifuged at 1,000 rpm for 5 min, washed once with PBS, and resuspended in 195 μL of Annexin V-FITC binding buffer. Subsequently, 5 μL of Annexin V-FITC and 10 μL of propidium iodide (PI) staining solution were added, and the mixture was gently vortexed. Following incubation at room temperature (20–25°C) for 10–20 min in the dark, the samples were immediately analyzed by flow cytometry. Data were processed using FlowJo software.

3.10 Reactive oxygen species (ROS) assay

S2 and Sf9 cells were seeded into 6-well plates at a density of 1 × 10^6 cells per well and cultured for 24 h. Cells were then treated with the MAT formulation at final concentrations of 75, 150, and 300 ng/mL for 12 h, with untreated cells or HcNPV treated cells serving as the control. After treatment, the culture medium was removed and the cells were incubated with DCFH-DA (10 μM, diluted in serum-free culture medium at 1:1000) at 37°C for 20 min in the dark. Following incubation, the cells were washed three times with serum-free medium to remove extracellular DCFH-DA. Fluorescence was visualized using a

confocal laser scanning microscope, and the intracellular ROS levels were reflected by the intensity of DCF fluorescence.

3.11 Mitochondrial membrane potential (*ΔΨm*) assay

S2 and Sf9 cells in the logarithmic growth phase were seeded into 6-well plates at a density of 1×10^6 cells per well and cultured for 24 h. Cells were then treated with the MAT formulation at final concentrations of 75, 150, and 300 ng/mL for 12 h, with untreated cells or HcNPV treated cells serving as the control. After treatment, the cells were fixed with 0.5 mL of fixative for 10 min, washed twice with PBS, and stained with Hoechst staining solution for 5 min. Following two additional PBS washes, the cells were incubated with 1 mL of JC-1 working solution (prepared by diluting JC-1 stock (200×) in JC-1 staining buffer at a ratio of 5 μL per 1 mL) at 37°C for 20 min in the dark. The staining solution was then removed, and the cells were washed twice with JC-1 staining buffer. Fresh culture medium was added, and fluorescence was visualized using a confocal laser scanning microscope. JC-1 monomers (green fluorescence) and J-aggregates (red fluorescence) were detected to assess mitochondrial membrane depolarization.

3.12 Larval midgut histopathology

Third- to fourth-instar *H. cunea* larvae were divided into three groups and orally administered the following treatments: sterile water (CK), native HcNPV suspension (300 ng/mL), and the DNA^{HcNPV}@LNP-CPP formulation (MAT, 300 ng/mL). Each treatment was applied to mulberry leaves at a volume of 20 μL, and larvae were fed ad libitum under controlled environmental conditions. After 24 h of feeding, larvae were dissected using sterilized fine forceps, and the midgut tissues were carefully excised. The midgut tissues were fixed in 4% paraformaldehyde for 24 h, dehydrated through a graded ethanol series (70%, 80%, 90%, 95%, and 100%), cleared in xylene, and embedded in paraffin. Serial sections were cut at a thickness of 5–8 μm using a microtome. Following deparaffinization and rehydration, the sections were processed for TUNEL fluorescence staining. Stained sections were mounted with neutral resin and observed under a light microscope to evaluate epithelial morphology, tissue architecture, and pathological changes across treatment groups. ImageJ was used to measure the thicknesses and for comparison among the treatments.

3.13 qRT-PCR analysis of viral gene expression

Third-instar *H. cunea* larvae were treated with native HcNPV suspension (positive control) or the DNA^{HcNPV}@LNP-CPP formulation (MAT). All treatments were normalized to an equivalent viral load of 1×10^5 PIBs/mL, with the MAT group dose calculated based on the amount of viral DNA used during nanoparticle preparation. Each treatment was performed in triplicate, with three larvae per replicate. Larvae were fed treated mulberry leaves as described above, and midgut tissues were dissected at 24 and 48 h post-feeding. Total RNA was extracted using TransZol reagent, assessed for integrity by 1% agarose gel electrophoresis, and quantified by UV spectrophotometry. First-strand cDNA was synthesized from 1 μg of total RNA using a reverse transcription kit with genomic DNA removal. qRT-PCR

was performed with a SYBR Green-based detection system on a real-time PCR instrument. The HcNPV genes *lef8*, *pe38*, *vp39*, *ie1*, *polh*, and *p10* were selected as targets, and the *H. cunea* ribosomal protein gene *RPL13* and elongation factor *EF-1α* served as dual internal reference genes for normalization. Amplification specificity was verified by melt curve analysis. Relative gene expression was calculated using the $2^{-\Delta\Delta Ct}$ method and normalized to the geometric mean of the two reference genes.

3.14 Indoor oral toxicity bioassay

Third-instar *H. cunea* larvae of uniform size and developmental stage were selected and placed individually in sterile plastic containers (7 cm × 7 cm × 11.2 cm). After an 8 h starvation period, larvae were fed fresh mulberry leaf discs (1 cm × 1 cm) coated with 10 μL of native HcNPV suspension or the DNA^{HcNPV}@LNP-CPP formulation, each normalized to an equivalent viral concentration of 1×10^5 PIBs/mL. Larvae that completely consumed the treated leaf discs within 24 h were transferred to fresh untreated mulberry leaves and reared under standard conditions (25 ± 1°C, 75 ± 5% relative humidity, 14L : 10D photoperiod). Each treatment was performed with three replicates of 20 larvae each. Mortality and signs of viral infection were recorded daily for 14 days, and the mean number of surviving and dead larvae per treatment was compared over time.

3.15 Field trials

Two independent field trials were conducted to evaluate the efficacy of the DNA^{HcNPV}@LNP-CPP formulation (MAT) against *H. cunea* under operational conditions. The first trial was performed in a mulberry (*Morus alba* cv. Wansangyou-1) plantation at the Anhui Academy of Agricultural Sciences Experimental Station (Changfeng County, Hefei, Anhui Province, China) from July 7 to July 21, 2025, with a single application. The second trial was carried out in an ash (*Fraxinus chinensis*) plantation in Maojiadian Village, Shanghe County, Jinan, Shandong Province, China, from September 3 to September 18, 2025, with two sequential applications spaced 5 days apart. Both trials employed the same three treatments: MAT (2.7×10^8 PIBs/mL, 270-fold dilution), native HcNPV (1.0×10^9 PIBs/mL, 1,000-fold dilution), and a water control. Treatments were applied using a backpack electric sprayer (3WBD-16, 0.4 MPa, 1 mm nozzle diameter) at a spray volume of 1 L per tree. In the first trial, a randomized complete block design with five replicates was used, each replicate plot covering 30 m^2 with 10 standard sampling trees selected for larval counting. In the second trial, four blocks were established with one replicate per treatment per block; each replicate plot covered 30 m^2 containing 8 ash trees, and pest-infested branches were enclosed with mesh netting for fixed-point monitoring. The number of live larvae was recorded before application and at regular intervals thereafter (every 2 days in the first trial; daily in the second trial). Multiple performance indicators were quantified, including larval counts, larval reduction rate, and corrected control efficacy, from which multi-factor response surfaces and spray-timing lag-day analysis were derived as the final graphical outputs.

3.16 Environmental stability assays

The native HcNPV, naked viral DNA, and the DNA^{HcNPV}@LNP-CPP formulation (MAT) were subjected to three environmental stress conditions: UVC irradiation (253.7 nm), elevated temperature (42°C), and natural outdoor exposure combining full-spectrum solar radiation with ambient summer temperatures. Samples were exposed for 0, 1, 6, 12, and 24 h, and the physical appearance of the formulations was visually inspected and photographed at each time point. Following stress treatment, viral DNA was extracted from native HcNPV and MAT using an alkaline lysis method, and the DNA concentration was quantified by NanoDrop spectrophotometry. The protective effect of the lipid encapsulation against the three stressors was assessed by comparing the residual DNA concentrations. The integrity of the viral genome was further verified by PCR amplification of the pe38 gene using the same protocol described above.

3.17 Stress-exposed formulation cytotoxicity assay

Naked HcNPV DNA, native HcNPV virions, and the DNA^{HcNPV}@LNP-CPP formulation (MAT) were subjected to the three environmental stress conditions described above. Following stress exposure, the samples were applied to S2 and Sf9 cells at MAT concentrations of 75, 150, and 300 ng/mL, with naked DNA and native HcNPV serving as controls. After 24 h of treatment, cell viability was assessed using the CCK-8 assay according to the manufacturer's protocol. Cell counting was performed using two image-based quantification strategies tailored to the distinct morphologies of the two cell lines. For S2 cells, which are small, round, and relatively uniform, a fully automated pipeline was employed using a Laplacian of Gaussian (LoG) blob detector with multi-scale peak detection, adaptive thresholding, and minimum-distance filtering (Data S1). For Sf9 cells, which exhibit irregular shapes and variable sizes, a supervised regression approach was adopted: regions of interest were manually annotated, and five features were extracted from each ROI. A Ridge regression model was trained on these features to predict cell counts and validated against manual counts (Data S2). Both methods were independently validated and yielded consistent estimates across replicates.

For flow cytometric analysis, stress-exposed samples were processed using the same PI staining protocol described above, and cell state distributions were analyzed with FlowJo software.

3.18 Non-target organism safety evaluation

The ecological safety of the DNA^{HcNPV}@LNP-CPP formulation was assessed across three complementary non-target models. In the first trial, third-instar fall armyworm larvae, a species naturally resistant to HcNPV infection, were randomly assigned to four treatment groups (30 larvae per group): sterile water (negative control), native HcNPV (1×10^5 PIBs/mL, positive control), blank LNP-CPP (vehicle control), and the DNA^{HcNPV}@LNP-CPP formulation (MAT, 1×10^5 PIB equivalents mL^{-1}). Larvae were starved for 12 h and then individually fed artificial diet cubes (5 mm^3) coated with 10 µL per larva of the respective treatment solution. After 24 h, the treated diet was replaced with untreated fresh diet. Larval survival and pupation were monitored over 8 days.

In the second trial, the safety assessment was extended to compare two CPP variants (LNP-C105Y and LNP-PAR) at low, mid, and high dosages, across three test organisms: fall armyworm larvae (10 per group), ladybug adults (10 per group), and zebrafish (30 per group). Treatments were applied as described above for the lepidopteran larvae. Ladybugs were maintained in Petri dishes, fed with aphids, and exposed to the formulations applied to the dish surface (10^5 PIB equivalents, 10 µL per insect). Zebrafish were exposed by the water immersion method in cylindrical glass tanks containing 2 L of water supplemented with 10 µL per fish of the respective formulation. Mortality was recorded daily over 6 days for fall armyworm and ladybug and over 5 days for zebrafish. At the end of the exposure period, zebrafish were dissected, and livers were photographed to compare gross morphology across treatment groups.

3.19 Statistical analysis

Data are presented as mean ± SEM unless otherwise noted. For comparisons between two groups, Student's t-test with Welch's correction was applied where parametric assumptions were met. For multiple-group comparisons, one-way analysis of variance (ANOVA) followed by Tukey's HSD post-hoc test was applied. When the assumption of equal variances was violated, the Kruskal–Wallis non-parametric test was used with Dunn's post-hoc correction. Count data were analyzed using the chi-square goodness-of-fit test. Survival data were analyzed by the Kaplan–Meier method, and differences among groups were assessed using the log-rank test and Cox regression. All statistical analyses were performed using GraphPad Prism 9.0 and Python, with a significance threshold of $\alpha = 0.05$.

3.20 Data availability

All data supporting the findings of this study are presented in the main text and the supplementary files.

Declarations

CRediT Author Contributions

Wen Zhao: Resources, Data curation, Validation, Formal analysis, Writing – original draft. Wen-Hao Hu: Methodology, Data curation, Validation, Formal analysis, Writing – original draft. Tao Lin: Methodology, Data curation, Supervision. Zi-Shang Li: Resources, Methodology, Data curation. Hui-Lan Mo: Data curation, Validation. Ye-Pin Yu: Supervision, Validation. Ping Hu: Resources, Validation. Ben-Shui Shu: Resources, Supervision. Jian-Ting Fan: Methodology, Supervision. Ding-Ze Mang: Resources, Validation. Chang-You Li: Resources, Methodology. Hong-Liang Yao: Resources, Methodology. Rui Tang: Resources, Methodology, Supervision, Formal analysis, Writing – original draft, Writing – review & editing.

Declaration of Competing Interests

The authors declare that they have no known competing financial interests or personal relationships that could have appeared to influence the work reported in this paper.

Acknowledgments

This work was supported by the National Key R&D Project of China (2023YFC2606900), the Young Talent Project of GDAS (2024GDASQNRC-0107), and the GDAS Special Project of Science and Technology Development (2024GDASZH-2024010102, 2022GDASZH-2022010106).

Declaration of Artificial Intelligence (AI) Use

During the preparation of this work, the authors used a large language model (LLM)-based AI assistant for language editing, grammar correction, and text polishing to improve the readability and clarity of the manuscript. The AI tool was also utilized to assist with programming and algorithm development for custom image-based cell counting and data processing pipelines. All scientific content, experimental design, data analysis, interpretation of results, and conclusions were generated entirely by the authors without AI involvement. After using this tool, the authors carefully reviewed and edited all generated content and take full responsibility for the accuracy, reproducibility, and originality of the final manuscript.

References

1. M. Martínez-Balerdi, J. Caballero, E. Aguirre, et al., Baculoviruses as Microbial Pesticides: Potential, Challenges, and Market Overview. *Viruses* 17, no. 7 (2025): 917.
2. W. H. Lau and E. Anggraini, Baculoviruses: Discovery, Interaction, and Application, in *Advances in Tropical Crop Protection* (Springer, Cham, 2024), 31–49.
3. F. Moscardi, Assessment of the Application of Baculoviruses for Control of Lepidoptera. *Annual Review of Entomology* 44, no. 1 (1999): 257–289.
4. G. F. Rohrmann, *Baculovirus Molecular Biology*, 4th ed. (National Center for Biotechnology Information, Bethesda, MD, 2019).
5. J. S. Cory and J. H. Myers, The Ecology and Evolution of Insect Baculoviruses. *Annual Review of Ecology, Evolution, and Systematics* 34, no. 1 (2003): 239–272.
6. M. Ghassemi, P. Painter, P. Painter, et al., *Bacillus thuringiensis*, Nucleopolyhedrosis Virus, and Pheromones: Environmental Considerations and Uncertainties in Large-Scale Insect Control. *Environment International* 9, no. 1 (1983): 39–49.
7. J. Liu, Q. He, X. Lin, and G. Smagghe, Recent Progress in Nanoparticle-Mediated RNA Interference in Insects: Unveiling New Frontiers in Pest Control. *Journal of Insect Physiology* (2025): 104884.
8. B. Boogaard, M. M. van Oers, and J. W. van Lent, An Advanced View on Baculovirus Per Os Infectivity Factors. *Insects* 9, no. 3 (2018): 84.
9. S. Yan, M.-Z. Yin, and J. Shen, Nanoparticle-Based Nontransformative RNA Insecticides for Sustainable Pest Control: Mechanisms, Current Status and Challenges. *Entomologia Generalis* 43 (2023): 21–30.

10. N. Mitter, E. A. Worrall, K. E. Robinson, et al., Clay Nanosheets for Topical Delivery of RNAi for Sustained Protection Against Plant Viruses. *Nature Plants* 3, no. 2 (2017): 16207.
11. Z. Zhang, H. Luo, X. Zhang, et al., Extracellular Vesicles Mimetic Design of Membrane Chimeric Nanovesicles for dsRNA Delivery in Spray-Induced Gene Silencing for Crop Protection. *ACS Nano*. 18, 47 (2024): 32468–32480.
12. O. Christiaens, S. Whyard, A. M. Vélez, and G. Smagghe, Double-Stranded RNA Technology to Control Insect Pests: Current Status and Challenges. *Frontiers in Plant Science* 11 (2020): 451.
13. X.-P. Kong, B.-H. Zhang, and J. Wang, Multiple Roles of Mesoporous Silica in Safe Pesticide Application by Nanotechnology: A Review. *Journal of Agricultural and Food Chemistry* 69, no. 24 (2021): 6735–6754.
14. J. Yong, M. Wu, B. J. Carroll, Z. P. Xu, and R. Zhang, Enhancing Plant Biotechnology by Nanoparticle Delivery of Nucleic Acids. *Trends in Genetics* 40, no. 4 (2024): 352–363.
15. G. V. Lowry, J. P. Giraldo, N. F. Steinmetz, et al., Towards Realizing Nano-Enabled Precision Delivery in Plants. *Nature Nanotechnology* 19, no. 9 (2024): 1255–1269.
16. X. Liu, Y. Zheng, S. Zhang, et al., Perylenediimide-Cored Cationic Nanocarriers Deliver Virus DNA to Kill Insect Pests. *Polymer Chemistry* 7, no. 22 (2016): 3740–3746.
17. X. Hou, T. Zaks, R. Langer, and Y. Dong, Lipid Nanoparticles for mRNA Delivery. *Nature Reviews Materials* 6, no. 12 (2021): 1078–1094.
18. M. J. Mitchell, M. M. Billingsley, R. M. Haley, M. E. Wechsler, N. A. Peppas, and R. Langer, Engineering Precision Nanoparticles for Drug Delivery. *Nature Reviews Drug Discovery* 20, no. 2 (2021): 101–124.
19. Q. Cheng, T. Wei, L. Farbiak, L. T. Johnson, S. A. Dilliard, and D. J. Siegwart, Selective Organ Targeting (SORT) Nanoparticles for Tissue-Specific mRNA Delivery and CRISPR–Cas Gene Editing. *Nature Nanotechnology* 15, no. 4 (2020): 313–320.
20. S. A. Dilliard, Q. Cheng, and D. J. Siegwart, On the Mechanism of Tissue-Specific mRNA Delivery by Selective Organ Targeting Nanoparticles. *Proceedings of the National Academy of Sciences* 118, no. 52 (2021): e2109256118.
21. X. Wang, S. Liu, Y. Sun, et al., Preparation of Selective Organ-Targeting (SORT) Lipid Nanoparticles (LNPs) Using Multiple Technical Methods for Tissue-Specific mRNA Delivery. *Nature Protocols* 18, no. 1 (2023): 265–291.
22. R. van der Meel, P. A. Wender, O. M. Merkel, et al., Next-Generation Materials for Nucleic Acid Delivery. *Nature Reviews Materials* 10, no. 7 (2025): 490–499.
23. Y. Lin, M. Li, Z. Luo, et al., Tissue-Specific mRNA Delivery and Prime Editing with Peptide–Ionizable Lipid Nanoparticles. *Nature Materials* 25, no. 1 (2026): 133–145.
24. M. Jayaraman, S. M. Ansell, B. L. Mui, et al., Maximizing the Potency of siRNA Lipid Nanoparticles for Hepatic Gene Silencing In Vivo. *Angewandte Chemie International Edition* 51, no. 34 (2012): 8529–8533.

25. J. A. Kulkarni, D. Witzigmann, S. B. Thomson, et al., The Current Landscape of Nucleic Acid Therapeutics. *Nature Nanotechnology* 16, no. 6 (2021): 630–643.
26. D. Aschmann, R. A. Knol, and A. Kros, Lipid-Based Nanoparticle Functionalization with Coiled-Coil Peptides for In Vitro and In Vivo Drug Delivery. *Accounts of Chemical Research* 57, no. 8 (2024): 1098–1110.
27. S. Renzi, L. Digiacomo, D. Pozzi, et al., Structuring Lipid Nanoparticles, DNA, and Protein Corona into Stealth Bionanoarchitectures for In Vivo Gene Delivery. *Nature Communications* 15, no. 1 (2024): 9119.
28. N. Huang, W. Wu, K. Yang, A. L. Passarelli, G. F. Rohrmann, and R. J. Clem, Baculovirus Infection Induces a DNA Damage Response That Is Required for Efficient Viral Replication. *Journal of Virology* 85, no. 23 (2011): 12547–12556.
29. M. Walter, M. Bresinsky, O. Zimmer, S. Pockes, and A. Goepferich, Conditional Cell-Penetrating Peptide Exposure as Selective Nanoparticle Uptake Signal. *ACS Applied Materials & Interfaces* 16, no. 29 (2024): 37734–37747.
30. S. V. Bleshøy, BPS2025—Varying Protein Corona Compositions Affect Endosomal Escape Propensities of Selective Organ-Targeting Lipid Nanoparticles. *Biophysical Journal* 124, no. 3 (2025): 593a.
31. S. J. Fletcher, P. T. Reeves, B. T. Hoang, and N. Mitter, A Perspective on RNAi-Based Biopesticides. *Frontiers in Plant Science* 11 (2020): 51.
32. S. Yan, B. Y. Ren, and J. Shen, Nanoparticle-Mediated Double-Stranded RNA Delivery System: A Promising Approach for Sustainable Pest Management. *Insect Science* 28, no. 1 (2021): 21–34.
33. G. Li, Q. He, E. B. Noruzi, et al., Enhancing Targeted Delivery of Pesticide on Superhydrophobic Wheat Leaves by Bioinspired Supramolecular Coacervates. *Advanced Functional Materials* 35, no. 52 (2025): e12143.
34. N. Saber, M. E. Senti, and R. M. Schiffelers, Lipid Nanoparticles for Nucleic Acid Delivery Beyond the Liver. *Human Gene Therapy* 35, no. 17–18 (2024): 617–627.
35. Q. Xue, J. Li, S. Vereecken, et al., Functionally Modified Graphene Oxide as an Alternative Nanovehicle for Enhanced dsRNA Delivery in Improving RNAi-Based Insect Pest Control. *Journal of Agricultural and Food Chemistry* 72, no. 41 (2024): 22512–22523.
36. A. I. Quilez-Molina, J. Niño Sanchez, and D. Merino, The Role of Polymers in Enabling RNAi-Based Technology for Sustainable Pest Management. *Nature Communications* 15, no. 1 (2024): 9158.
37. I. Schneider, Cell Lines Derived from Late Embryonic Stages of *Drosophila melanogaster*. *Development* 27, no. 2 (1972): 353–365.
38. J. L. Vaughn, R. H. Goodwin, G. J. Tompkins, and P. McCawley, The Establishment of Two Cell Lines from the Insect *Spodoptera frugiperda* (Lepidoptera; Noctuidae). *In Vitro* 13, no. 4 (1977): 213–217.

Table

Table 1. Key biological materials and reagents used in this study.

Name	Resource	Identifier
Hyphantria cunea nucleopolyhedrovirus (HcNPV)	Laboratory stock, Qingdao Agricultural University, Shandong, China	N/A
Sf9 cells (*Spodoptera frugiperda* ovary)	Wuhan Pricella Biotechnology, Hubei, China	CL-0205
S2 cells (*Drosophila melanogaster* embryo)	iCell Bioscience, Shanghai, China	iCell-c041
Schneider's *Drosophila* Medium (with L-glutamine, without phenol red)	iCell Bioscience, Shanghai, China	iCell-0018-500mL
TNM-FH Insect Medium	Wuhan Pricella Biotechnology, Hubei, China	PM52010-500mL
Penicillin-Streptomycin Solution (100×)	Wuhan Pricella Biotechnology, Hubei, China	PB180120-125mL
Premium Fetal Bovine Serum	Wuhan Pricella Biotechnology, Hubei, China	164210-50-50mLx10
0.25% Trypsin Solution (with EDTA and phenol red, in D-Hanks' solution)	Wuhan Pricella Biotechnology, Hubei, China	PB180226-125mL
L-Glutamine Solution (200 mM), 100×	Wuhan Pricella Biotechnology, Hubei, China	PB180420-100mL
Corning petri dish	Corning Incorporated, NY, USA	430166
Enhanced Cell Counting Kit-8 (CCK-8)	Wuhan Pricella Biotechnology, Hubei, China	P-CA-001
Enhanced Mitochondrial Membrane Potential Assay Kit (JC-1)	Beyotime, Shanghai, China	C2003S
Cell Cycle and Apoptosis Detection Kit	Beyotime, Shanghai, China	C1052
Annexin V-FITC Apoptosis Detection Kit	Beyotime, Shanghai, China	C1062L
Apoptosis-Hoechst Staining Kit	Beyotime, Shanghai, China	C0003
Reactive Oxygen Species (ROS) Assay Kit	Beyotime, Shanghai, China	S0033
Phosphate Buffered Saline (PBS), 1×	Wuhan Pricella Biotechnology, Hubei, China	PB180327
DLin-MC3-DMA	Macklin Biochemical, Shanghai, China	D302656
DSPC (1,2-distearoyl-sn-glycero-3-phosphocholine)	Macklin Biochemical, Shanghai, China	D100513
Cholesterol	Macklin Biochemical, Shanghai, China	C100274

DSPE-PEG_{2000}-Mal (1,2-distearoyl-sn-glycero-3-phosphoethanolamine-N-[maleimide(polyethylene glycol)-2000])	Aladdin, Shanghai, China	D163619
DSPE-PEG_{2000}-NHS	Yusi Pharmaceutical, Chongqing, China	YEN-1002
DOTAP (1,2-dioleoyl-3-trimethylammonium-propane)	Aladdin, Shanghai, China	D110875
C105Y peptide	Jietai Biotechnology, Nanjing, China	JT-209069
Pardaxin peptide (PAR)	Zhuantai Peptide, Hangzhou, China	AP18299
Virus Concentration Kit	Beyotime, Shanghai, China	C2901L
TransZol Up Plus RNA Kit	TransGen Biotech, Beijing, China	ET111
TransScript® One-step gDNA Removal and cDNA Synthesis SuperMix for qPCR	TransGen Biotech, Beijing, China	AT311
TransStart® Top Green qPCR SuperMix	TransGen Biotech, Beijing, China	AQ131

Figures

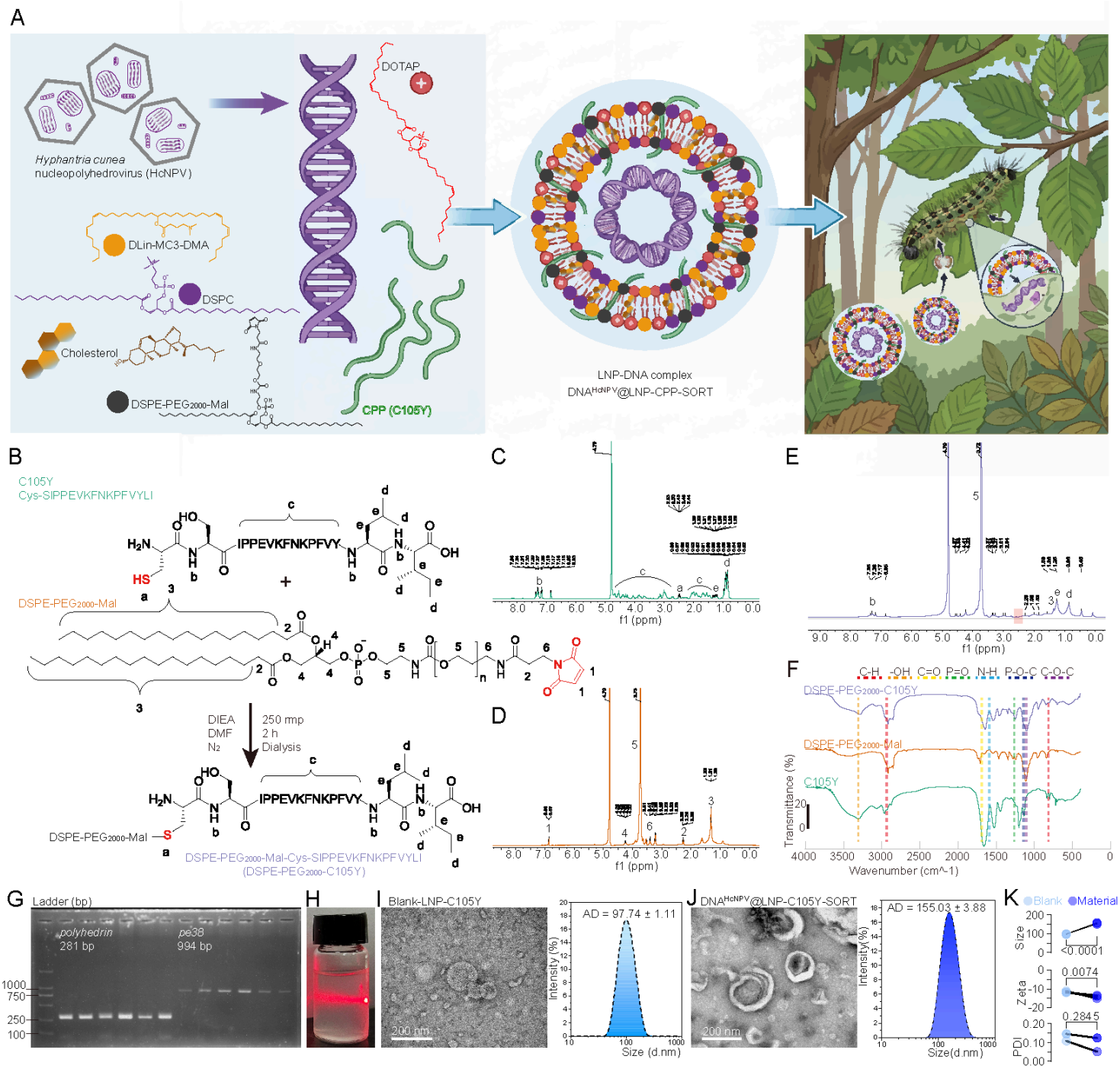


Figure 1

Design, synthesis, and characterization of DNA^{HcNPV}@LNP-CPP-SORT. (**A**) Schematic illustration of the nanoparticle platform, composed of HcNPV genomic DNA, DLin-MC3-DMA, DSPC, cholesterol, DSPE-PEG$_{2000}$-Mal, the CPP ligand (C105Y), and the SORT molecule DOTAP. (**B**) Reaction scheme for the synthesis of DSPE-PEG$_{2000}$-C105Y via Michael addition between the maleimide group of DSPE-PEG$_{2000}$-Mal and the N-terminal cysteine thiol of C105Y. (C–E) ^{1}H NMR spectra (400 MHz, D_2O) of C105Y (**C**), DSPE-PEG$_{2000}$-Mal (**D**), and DSPE-PEG$_{2000}$-C105Y (**E**). The red box in (**E**) highlights the disappearance of the characteristic signal of the C105Y *α*-proton (δ ~2.5 ppm), confirming covalent conjugation. (**F**) FTIR

spectra of C105Y, DSPE-PEG_{2000}-Mal, and DSPE-PEG_{2000}-C105Y. (**G**) PCR verification of the HcNPV strain by amplification of the *polyhedron* (~281 bp) and *pe38* (~994 bp) genes, resolved by agarose gel electrophoresis. (**H**) Tyndall effect of the prepared DNA^{HcNPV}@LNP-CPP-SORT formulation, indicating the presence of colloidal nanoparticles. (**I**) TEM image and hydrodynamic diameter distribution of Blank-LNP-C105Y. AD, average diameter ± SEM. (**J**) TEM image and hydrodynamic diameter distribution of DNA^{HcNPV}@LNP-CPP-SORT. (**K**) Comparison of particle size, zeta potential, and polydispersity index (PDI) between Blank-LNP-C105Y and DNA^{HcNPV}@LNP-CPP-SORT. P values (unpaired t-test) are indicated in each panel.

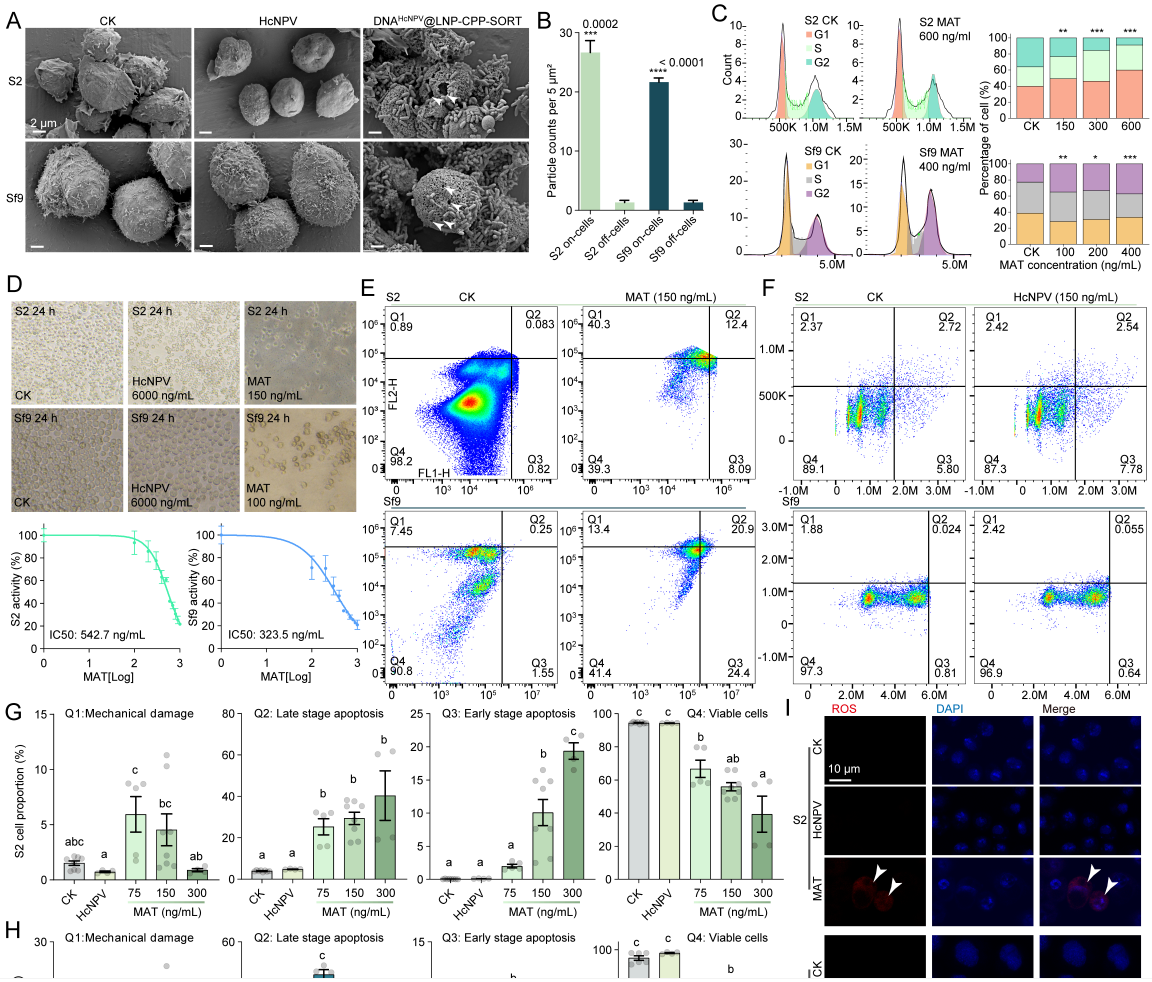


Figure 2

Cellular uptake, cytotoxicity, and mechanistic basis of MAT-mediated enhancement in S2 and Sf9 cells. (**A**) Representative SEM images showing particle accumulation and membrane penetration of the MAT formulation on S2 and Sf9 cells, compared with CK and native HcNPV. White arrows indicate perforations on the cell membrane induced by MAT. (**B**) Quantification of nanoparticle counts within randomly selected 5 μm^2 regions of interest positioned on-cells versus off-cells. Asterisks denote

significant differences, with exact P values provided (unpaired t-test). (**C**) Flow cytometric analysis of cell cycle distribution in S2 and Sf9 cells treated with MAT compared with CK. Significant differences in cell cycle stage distributions were determined by chi-square tests (S2: 150 ng/mL, $\chi^2 = 11.08$, $P = 0.0039$; 300 ng/mL, $\chi^2 = 34.19$, $P < 0.001$; 600 ng/mL, $\chi^2 = 67.69$, $P < 0.001$; Sf9: 100 ng/mL, $\chi^2 = 12.88$, $P = 0.0016$; 200 ng/mL, $\chi^2 = 8.83$, $P = 0.012$; 400 ng/mL, $\chi^2 = 17.77$, $P = 0.00014$). (**D**) Upper panels: bright-field images of CK, HcNPV, and MAT-treated cells at 24 h. Lower panels: dose-response curves and IC_{50} values for MAT in S2 and Sf9 cells determined by CCK-8 assay ([Inhibitor] vs. normalized response with variable slope; S2: $R^2 = 0.96$; Sf9: $R^2 = 0.94$). (**E**, **F**) Representative flow cytometric apoptosis maps (Q1–Q4 quadrants) for S2 and Sf9 cells treated with CK vs. MAT (**E**, 150 ng/mL) or CK vs. HcNPV (**F**, 150 ng/mL). Q1, mechanical damage; Q2, late apoptosis/necrosis; Q3, early apoptosis; Q4, viable cells. (**G**) Quantification of cell state proportions (Q1–Q4) in S2 cells across CK, HcNPV, and three MAT dosages. Different lowercase letters indicate significant differences (one-way ANOVA with Tukey HSD or Kruskal–Wallis test; Q1: $K_{4,24} = 17.22$, $P = 0.0018$; Q2: $F_{4,24} = 19.98$, $P < 0.0001$; Q3: $F_{4,24} = 22.50$, $P < 0.0001$; Q4: $F_{4,24} = 10.90$, $P < 0.0001$). (**H**) Quantification of cell state proportions in Sf9 cells (Q1: $F_{4,17} = 5.59$, $P < 0.0001$; Q2: $F_{4,17} = 11.41$, $P < 0.0001$; Q3: $F_{4,17} = 6.43$, $P < 0.0001$; Q4: $F_{4,17} = 10.12$, $P < 0.0001$). (**I**) Confocal fluorescence images of intracellular ROS production. Nuclei were stained with DAPI (blue), and ROS signals were detected with DCFH-DA (red). White arrows indicate robust ROS accumulation induced by MAT in S2 and Sf9 cells, in contrast to negligible signals in CK and HcNPV groups. (**J**) Flow cytometric histograms (upper panel) and quantification (lower panel) of ROS levels in S2 cells. Different lowercase letters indicate significant differences among CK and 75, 150, and 300 ng/mL MAT ($F_{3,9} = 11.89$, $P < 0.0001$). (**K**) Histograms and quantification of ROS levels in Sf9 cells ($F_{3,8} = 1.00$, $P < 0.0001$). (**L**) Confocal images of JC-1 staining showing mitochondrial membrane potential ($\Delta\Psi m$) in S2 and Sf9 cells treated with CK, HcNPV, or MAT. Red fluorescence (Cy3 channel) represents J-aggregates in healthy mitochondria; green fluorescence (EGFP channel) indicates JC-1 monomers released upon mitochondrial depolarization. Yellow signals in the merge channel reflect impaired mitochondrial activity induced by MAT. (**M**) Flow cytometric histograms (upper panel) and quantification (lower panel) of EGFP fluorescence intensity. Different lowercase letters indicate significantly higher EGFP intensity in MAT-treated groups (75–300 ng/mL) compared with CK, positive control, and HcNPV ($F_{5,15} = 2.65$, $P < 0.0001$).

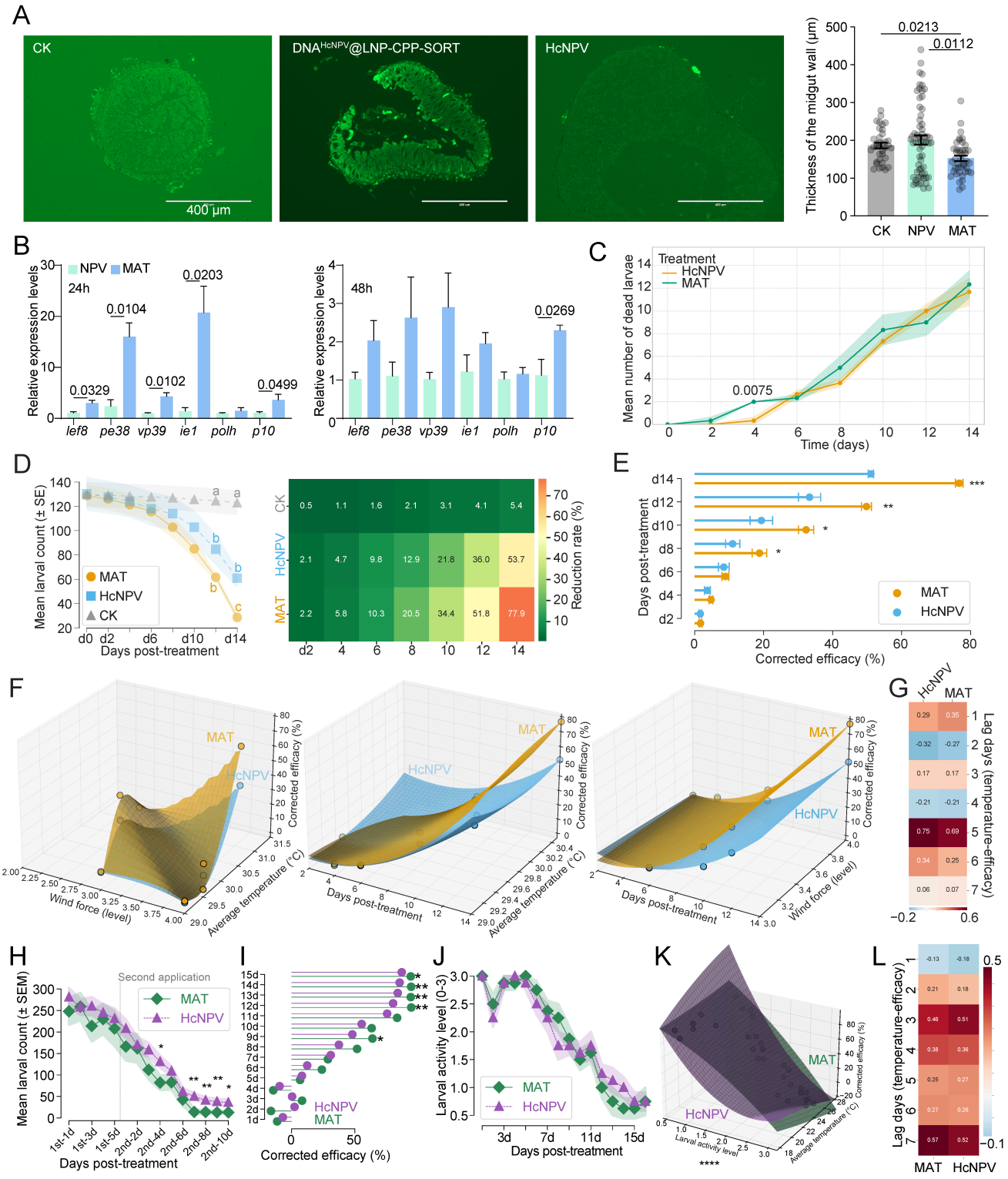


Figure 3

In vivo* efficacy and field performance of the MAT formulation against *H. cunea. (**A**) Representative histological sections (H&E staining) of larval midgut tissues at 24 h post-treatment, showing disruption of the peritrophic matrix and thinning of the midgut epithelium induced by the MAT formulation compared with CK and native HcNPV. (**B**) Quantification of midgut epithelial thickness across the three treatment groups. Significant thinning was observed in MAT-treated larvae (Kruskal–Wallis test, χ^2=

10.33, df = 2, P = 0.0057, multiple comparison P values provided above the bars). (**C**) qRT-PCR analysis of viral gene expression (*lef8*, *pe38*, *vp39*, *ie1*, *polh*, *p10*) in the larval midgut at 24 h (left) and 48 h (right) post-treatment. P values are shown above bars where significantly higher expression was detected in MAT relative to native HcNPV. (**D**) Indoor larval bioassay comparing cumulative mortality between MAT and native HcNPV over 14 days. Data points represent mean ± SEM (shaded bands). A significant difference was observed at day 4 (Welch's t-test, t = 2.83, df = 4). (**E**) Field trial I (mulberry, single application). Left: larval population dynamics in MAT-, HcNPV-, and CK-treated plots. Different lowercase letters indicate significant differences (day 12: $F_{2,12}$ = 11.90, P = 0.0014; day 14: $F_{2,12}$ = 43.20, P < 0.0001). Right: heatmap of larval reduction rates at each monitoring time point. (**F**) Corrected control efficacy of MAT versus native HcNPV in the first field trial. Asterisks denote significantly higher efficacy of MAT (Welch's t-test; day 8: t = 2.64, df = 8, P = 0.030; day 10: t = 3.29, df = 7, P = 0.013; day 12: t = 4.66, df = 5, P = 0.0042; day 14: t = 18.84, df = 7, P < 0.0001). (**G**) Three-dimensional response surface plots showing the relationships among corrected efficacy, wind force, temperature, and days post-treatment for MAT and native HcNPV. (**H**) Lag-day correlation analysis between temperature and efficacy, presented as color-coded heatmaps for MAT and native HcNPV. (I) Field trial II (ash trees, two sequential applications). Larval counts in MAT- and NPV-treated plots. Asterisks indicate significantly lower counts in MAT (Welch's t-test; day 4 post-second-application: t = 2.22, df = 13, P = 0.044; day 7: t = 3.77, df = 13, P = 0.0024; day 8: t = 3.10, df = 12, P = 0.0090; day 9: t = 3.32, df = 10, P = 0.0075; day 10: t = 2.84, df = 10, P = 0.018). (**J**) Corrected control efficacy in the second field trial. Asterisks denote significantly higher efficacy of MAT (Welch's t-test; day 9: t = 2.22, df = 13, P = 0.044; day 12: t = 3.80, df = 13, P = 0.0023; day 13: t = 3.10, df = 12, P = 0.0090; day 14: t = 3.29, df = 10, P = 0.0080; day 15: t = 2.78, df = 10, P = 0.020). (**K**) Larval activity levels over time in MAT- and HcNPV-treated plots. (**L**) Response surface analysis showing corrected efficacy as a function of temperature and larval activity. Significant correlations were observed for both treatments between efficacy and larval activity (MAT: R^2 = 0.955, P < 0.0001; HcNPV: R^2 = 0.938, P < 0.0001). (**M**) Lag-day correlation analysis for the second field trial, displayed as color-coded heatmaps.

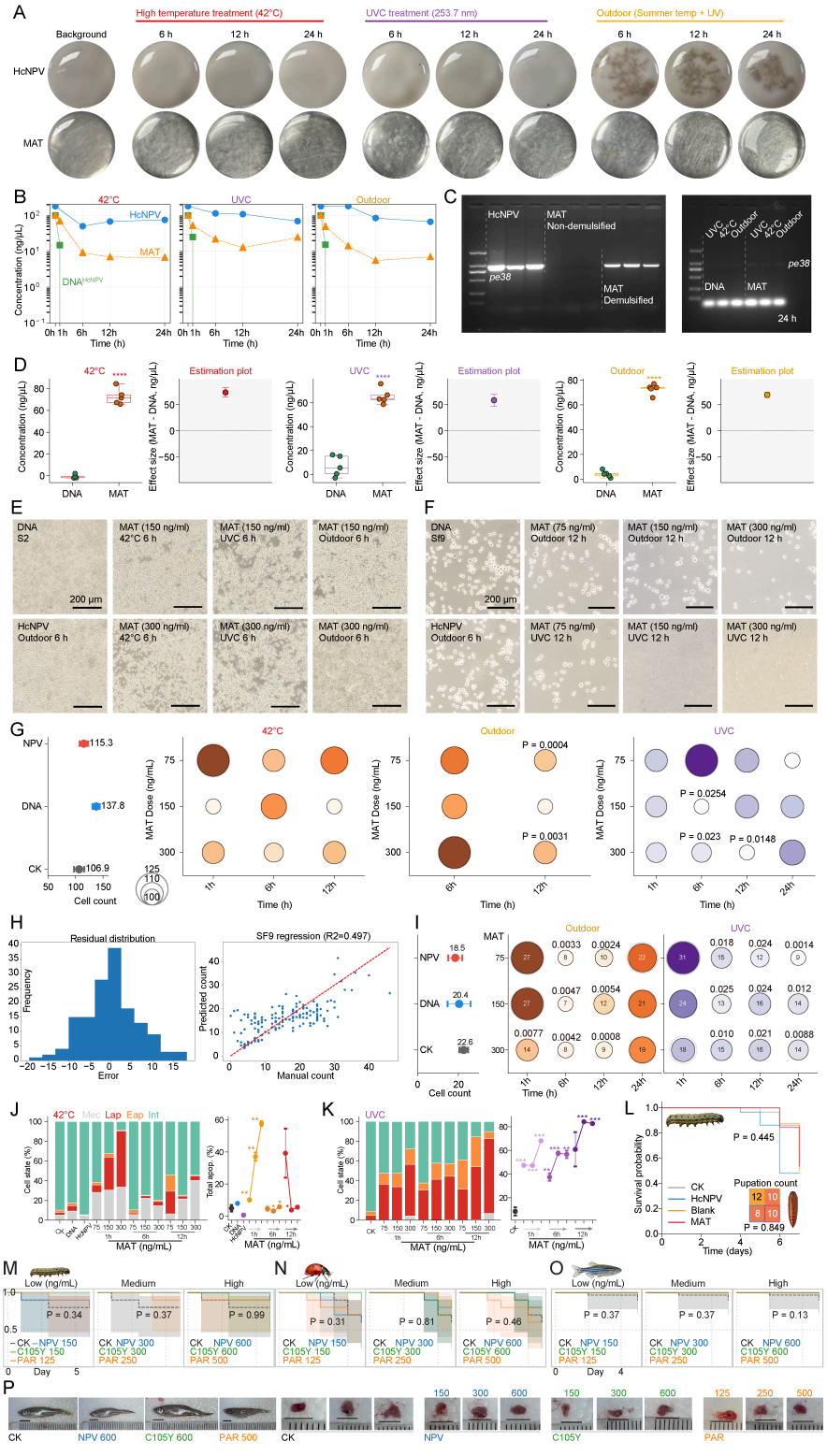


Figure 4

Environmental stability and ecological safety profile of the MAT formulation. (**A**) Visual appearance of native HcNPV and MAT formulations following exposure to elevated temperature (42°C), UVC irradiation (253.7 nm), and natural outdoor conditions for 6, 12, and 24 h. (**B**) Residual DNA concentration (ng/μL) measured over 24 h of stress exposure for naked HcNPV DNA, native HcNPV, and MAT under the three stress conditions. (**C**) Left: PCR amplification of the *pe38*gene from native HcNPV, intact (non-

demulsified) MAT, and demulsified MAT. Right: PCR detection of *pe38* in naked DNA and MAT following 24 h of exposure to the three stress treatments. (**D**) Comparison of residual DNA concentration between naked DNA and MAT after stress exposure. Asterisks indicate significantly higher DNA retention in MAT (Welch's t-test; 42°C: t = 21.58, df = 8, P < 0.0001; UVC: t = 12.08, df = 8, P < 0.0001; outdoor: t = 30.87, df = 8, P < 0.0001). Estimation plots are shown to the right of each panel. (**E**, **F**) Bright-field microscopy images of S2 (**E**, 6 h) and Sf9 (**F**, 12 h) cells treated with stress-exposed naked DNA, native HcNPV, or MAT (75–300 ng/mL). (**G**) Bubble plot summarizing S2 cell counts across treatments (CK, DNA, HcNPV, MAT) under the three stress conditions (42°C, outdoor, UVC) at 1, 6, and 12 h, and at MAT concentrations of 75, 150, and 300 ng/mL. Exact P values are shown above the bubbles where significant decreases were observed. (**H**) Validation of the Sf9 cell counting algorithm. Left: residual distribution plot. Right: regression between manual counts and predicted counts (Ridge regression). (**I**) Bubble plot summarizing Sf9 cell counts under outdoor and UVC stress conditions at 1, 6, 12, and 24 h with MAT at 75, 150, and 300 ng/mL. Exact P values denote significant decreases relative to controls. (**J**) Flow cytometric analysis of cell cycle distribution in S2 cells treated with CK, DNA, HcNPV, or MAT (75, 150, 300 ng/mL) under 42°C stress for 1, 6, and 12 h. Asterisks indicate significant redistribution of cell cycle phases (MAT75, 1 h: t = 85.15, P = 0.0056; MAT150, 1 h: t = 70.03, P = 0.0017; MAT300, 1 h: t = 222.05, P = 0.0020; MAT150, 6 h: t = 19.21, P = 0.015; MAT300, 6 h: t = 11.26, P = 0.039; MAT150, 12 h: t = 13.78, P = 0.032). (**K**) Cell cycle distribution in S2 cells treated with UVC-exposed CK or MAT (75, 150, 300 ng/mL) for 1, 6, and 12 h. Asterisks indicate significant differences (MAT75, 1 h: t = 28.06, P < 0.0001; MAT150, 1 h: t = 26.92, P < 0.0001; MAT300, 1 h: t = 45.07, P < 0.0001; MAT75, 6 h: t = 11.16, P = 0.0096; MAT150, 6 h: t = 27.90, P < 0.0001; MAT300, 6 h: t = 18.81, P = 0.0034; MAT150, 12 h: t = 53.73, P < 0.0001; MAT300, 12 h: t = 52.48, P < 0.0001). (**L**) Oral toxicity of MAT toward non-target fall armyworm larvae over 7 days, compared with CK, native HcNPV, and blank LNP. P values are provided for survival probability and pupation counts; no significant differences were detected. (**M**) Comparative oral toxicity of two CPP variants (LNP-C105Y and LNP-PAR) versus CK and HcNPV in fall armyworm larvae over 6 days at low, medium, and high doses. P values for survival probability are indicated; no significant differences were observed. (**N**) Toxicity of two CPP formulations versus CK and HcNPV toward ladybug adults over 6 days. Exact P values are given for the low, medium, and high dose panels. (**O**) Toxicity of two CPP formulations versus CK and HcNPV toward zebrafish over 5 days. P values are given for the low, medium, and high dose panels. (**P**) Gross morphology of zebrafish and excised livers across the four treatment groups and dose levels. Scale bar: 5 mm.

Supplementary Files

This is a list of supplementary files associated with this preprint. Click to download.

- S.I..docx
- DataS1.txt
- DataS2.txt